# Global distribution of bedrock exposures on Mars using THEMIS high-resolution thermal inertia

C. S. Edwards,[1] J. L. Bandfield,[2] P. R. Christensen,[1] and R. L. Fergason[3]

Received 12 February 2009; revised 26 June 2009; accepted 21 July 2009; published 4 November 2009.

[1] We investigate high thermal inertia surfaces using the Mars Odyssey Thermal Emission Imaging System (THEMIS) nighttime temperature images (100 m/pixel spatial sampling). For this study, we interpret any pixel in a THEMIS image with a thermal inertia over 1200 J $m^{-2}$ $K^{-1}$ $s^{-1/2}$ as "bedrock" which represents either in situ rock exposures or rock-dominated surfaces. Three distinct morphologies, ranked from most to least common, are associated with these high thermal inertia surfaces: (1) valley and crater walls associated with mass wasting and high surface slope angles; (2) floors of craters with diameters >25 km and containing melt or volcanics associated with larger, high-energy impacts; and (3) intercrater surfaces with compositions significantly more mafic than the surrounding regolith. In general, bedrock instances on Mars occur as small exposures (less than several square kilometers) situated in lower-albedo (<0.18), moderate to high thermal inertia (>350 J $m^{-2}$ $K^{-1}$ $s^{-1/2}$), and relatively dust-free (dust cover index <0.95) regions; however, there are instances that do not follow these generalizations. Most instances are concentrated in the southern highlands, with very few located at high latitudes (poleward of 45°N and 58°S), suggesting enhanced mechanical breakdown probably associated with permafrost. Overall, Mars has very little exposed bedrock with only 960 instances identified from 75°S to 75°N with likely <3500 $km^2$ exposed, representing $\ll$1% of the total surface area. These data indicate that Mars has likely undergone large-scale surface processing and reworking, both chemically and mechanically, either destroying or masking a majority of the bedrock exposures on the planet.

**Citation:** Edwards, C. S., J. L. Bandfield, P. R. Christensen, and R. L. Fergason (2009), Global distribution of bedrock exposures on Mars using THEMIS high-resolution thermal inertia, *J. Geophys. Res.*, *114*, E11001, doi:10.1029/2009JE003363.

## 1. Introduction

[2] Compositional mapping of the surface of Mars through the use of spectroscopic data (e.g., Thermal Emission Spectrometer (TES), Thermal Emission Imaging System (THEMIS), Compact Reconnaissance Imaging Spectrometer for Mars (CRISM)) has provided many insights into the history and evolution of the Martian surface. However, the mapping of surface composition from orbit leaves open many questions concerning the nature of the exposed materials. The extent of alteration or comminution and what the relationship is between the exposed materials and primary source rock is often unknown. Identification of in situ rock outcrops where the original geologic contexts are largely undisturbed may provide the most direct compositional information about the formation of the crust and its subsequent development. Through the use of high-resolution thermal inertia data, we have classified and mapped the global distribution of bedrock or bedrock-dominated surfaces on Mars. These localities are of great interest as they represent the least mechanically, and possibly mineralogically, altered primary crustal materials exposed on the Martian surface.

[3] In addition to locating geologically significant rock outcrops, other constraints on Martian history can be developed based on these data. For instance, the global distribution of high thermal inertia surfaces provides insight into the role of climate related processes on regolith development and evolution in high-latitude regions. The distribution of bedrock provides insight into several outstanding questions about the evolutionary history of Mars, including the crustal magmatic and alteration history and the rate of regolith production from either mechanical and/or chemical weathering.

[4] Several distinctive global thermal inertia units have been identified on Mars using TES surface temperature data (for a detailed discussion, see *Mellon et al.* [2000], *Putzig et al.* [2005], and *Putzig and Mellon* [2007b]). From these data, the entire planet has been mapped at a maximum spatial resolution of 20 pixels/degree, which is a significant improvement in spatial sampling over the 0.5–2 pixel/degree Viking Infrared Thermal Mapper (IRTM) thermal inertia mapping [*Christensen and Moore*, 1992; *Kieffer et al.*, 1977; *Palluconi and Kieffer*, 1981]. THEMIS data allow for mapping thermophysical and compositional properties of a surface at a spatial sampling of 100 m/pixel with regional

[1]Mars Space Flight Facility, School of Earth and Space Exploration, Arizona State University, Tempe, Arizona, USA.
[2]Department of Earth and Space Sciences, University of Washington, Seattle, Washington, USA.
[3]U.S. Geological Survey, Flagstaff, Arizona, USA.


0148-0227/09/2009JE003363

and global context [*Christensen et al.*, 2003, 2004, 2007], a significant improvement over the ~3 km by 6 km sampling of TES. This higher spatial sampling lessens the effects of subpixel mixing by different terrain types and allows for a more realistic determination of the local geology of study areas. *Fergason et al.* [2006a] have applied this data to a variety of locations including the interior layered deposits within Hebes Chasma, locations containing various aeolian bed forms, and the Nili Patera caldera, which illustrate the types of surfaces associated with a variety of thermal inertia values.

[5] Several early studies have focused on high thermal inertia material. For example, *Christensen* [1983] discusses the relatively high thermal inertia material inside craters. Dark visual "splotches" corresponded with a high thermal inertia surface and *Christensen* [1983] notes that approximately one fourth of all craters on Mars exhibit these features. The concentration of this relatively high thermal inertia material (typically ~300–400 J $m^{-2}$ $K^{-1}$ $s^{-1/2}$) in large (>25 km in diameter) craters is likely due to the preferential accumulation of coarse sand particles. Therefore, these deposits were interpreted to be mobile sediment or a remnant lag, which has been preferentially sorted to include only larger particles (effective grain size of up to 1 cm) [*Christensen*, 1983]. One limitation of this early study was the low resolution of the IRTM data that allowed for only investigation of craters greater than 25 km diameter, to insure that only the floor of the crater influenced the observed thermal data. These low-resolution data effectively integrate thermal inertia values over ~625 $km^2$ or greater area that is likely a mixture of surfaces with a range of thermal inertia values, leaving the possibility that there may be material with very high thermal inertia present but unresolved.

[6] More recent investigations using higher-resolution TES and THEMIS data have also focused on high-inertia surfaces. Areas with very high thermal inertia values have been identified in TES data, such as the rim of Isidis Basin, which has values of >800 J $m^{-2}$ $K^{-1}$ $s^{-1/2}$ [*Christensen et al.*, 2005b; *Putzig et al.*, 2005; *Putzig and Mellon*, 2007b]. Several other areas (e.g., Argyre Planitia, Acidalia, Valles Marineris, etc.) with similar thermal inertia values have been identified and are consistent with coarse grained, highly indurated materials, high rock abundance, and bedrock exposures [*Putzig et al.*, 2005]. THEMIS nighttime temperature data have been used to calculate thermal inertia and have yielded even higher values than those described by *Putzig et al.* [2005] for several locations on Mars. For example, olivine-rich basalt bedrock with thermal inertia values of >1200 J $m^{-2}$ $K^{-1}$ $s^{-1/2}$ in Ganges and Eos chasmas was identified and mapped using THEMIS multispectral data [*Edwards et al.*, 2008]. High thermal inertia, olivine-rich surfaces have also been identified in Nili Fossae, Nili Patera Ares Valles and Argyre Planitia [*Bandfield and Rogers*, 2008; *Christensen et al.*, 2005a; *Hamilton and Christensen*, 2005; *Mustard et al.*, 2007; *Rogers et al.*, 2005]. Although these studies have identified high thermal inertia units, they generally focused on isolated regions.

[7] The focus of this study is to map the global distribution (between ±75°N) of very high thermal inertia surfaces (defined here as >1200 J $m^{-2}$ $K^{-1}$ $s^{-1/2}$) on Mars and determine the associated morphologies and geologic contexts of these surfaces. The combination of thermophysical, morphological, and mineralogical data sets provides a more complete picture of the geologic contexts and formation mechanisms of these surfaces than could be achieved through isolated analyses.

[8] Lower maximum thermal inertias of 800 J $m^{-2}$ $K^{-1}$ $s^{-1/2}$ have been used previously [*Mellon et al.*, 2000; *Putzig et al.*, 2005] to identify regions of high thermal inertia. More recently, *Putzig and Mellon* [2007b] have calculated thermal inertia values for TES data using a thermal model with lookup table values that range from 5 to 5000 J $m^{-2}$ $K^{-1}$ $s^{-1/2}$. These data show concentrations of high thermal inertia surfaces (as defined in this study) near Valles Marineris and some instances to the north of Syrtis Major near Nilosyrtis Mensae. In this study, we will show that areas previously identified with high thermal inertia values in TES data will also contain instances of high thermal inertia surfaces of interest in this study, for example in the walls of Valles Marineris.

[9] The interpretation of a high thermal inertia surface is ambiguous as in situ bedrock and surfaces dominated by rocks >~30 cm in diameter have similar temperatures. High-resolution visible images such as those acquired by the High Resolution Imaging Science Experiment (HiRISE) [*McEwen et al.*, 2007] can be used to identify the morphologic context of the surfaces. These images show that high thermal inertia surfaces can be both boulder fields and bedrock-dominated surfaces. If the surface is dominated by rocks and boulders, it is likely that these materials are largely immobile, have experienced limited mechanical processing, and imply a similar significance as in situ bedrock dominated surfaces. For brevity, the term "bedrock" will be used throughout this work to represent all of these surface types without attempting to distinguish between them.

## 2. Method

[10] Thermal inertia is defined as $I = (k\rho c)^{1/2}$, where k is the thermal conductivity, $\rho$ is the bulk density of the material, and c is specific heat. On Mars thermal inertia is strongly controlled by the thermal conductivity [*Jakosky*, 1986; *Kieffer et al.*, 1973; *Presley and Christensen*, 1997a, 1997b, 1997c], which can be related to an effective particle size [*Kieffer et al.*, 1973] and is used to quantitatively determine the physical properties of the upper several decimeters of surface material. Under Martian environmental conditions, surfaces with lower thermal inertia are interpreted as having smaller particle sizes. Quantitative laboratory studies have established relationships between particle size and conductivity [*Presley and Christensen*, 1997a, 1997b; *Presley and Craddock*, 2006] and can be applied to spacecraft data from Mars [e.g., *Fergason et al.*, 2006b; *Kieffer et al.*, 1973]. Surface properties, such as albedo and slope, in addition to the effects of horizontal and vertical heterogeneity, also influence the derivation and interpretation of thermal inertia. For a more detailed discussion of the influence of these factors on the derived thermal inertia see *Fergason et al.* [2006a] and *Putzig and Mellon* [2007a, 2007b].

### 2.1. Data Set Description and Thermal Model Application

[11] The thermal infrared imager on THEMIS consists of a 9 spectral channel, 320 by 240 element uncooled, micro-

bolometer array that covers a wavelength range of 6.7 to 14.8 $\mu$m. It has 100 m/pixel spatial sampling from the ~420 km altitude orbit of the 2001 Mars Odyssey spacecraft. A detailed description of the instrument is provided by *Christensen et al.* [2004]. Due to the nearly global coverage and high spatial resolution, THEMIS infrared data provide an excellent means to identify exposures of and map the distribution of bedrock on Mars.

[12] Data selection was restricted to surface temperatures >160 K to avoid interfering effects from seasonal $CO_2$ frost. Additional constraints were placed on regions poleward of 60°latitude by limiting the seasons to late summer (~100–120° $L_s$ in the North and ~290–310° $L_s$ in the South) to avoid times when $CO_2$ frost might be present on the surface. This seasonal restriction also minimizes the effects of near surface water ice on derived surface cover thermal inertia [*Bandfield*, 2007; *Bandfield and Feldman*, 2008]. Other constraints used on all data in this work included limiting the study to nadir-looking images with <10% data dropouts, nighttime data with the sun at least 5° below the horizon (incidence angle of >95°), and local solar times of 0200–0630. No data were selected poleward of 75° latitude as these regions are dominated by polar processes. No exposed bedrock was identified poleward of ~50° latitude in this study.

[13] Calibrated radiance data [*Christensen et al.*, 2004], corrected for focal plane temperature drift [*Bandfield et al.*, 2004], were converted to minimum, maximum and average temperatures for each framelet, or 256-line segment of the image. The radiance data were converted to brightness temperatures using the 7.9–12.6 $\mu$m THEMIS bands 3–9 for images with warm brightness temperatures (>240 K) and only the 12.6 $\mu$m THEMIS band 9 for cooler images (<240 K) using a lookup table of Planck radiances convolved with the THEMIS filter response for each band. The highest brightness temperature from each band for each pixel is chosen to create the one band estimated surface kinetic temperature image. Typically, at the wavelengths covered by THEMIS band 9, surface emissivity is high (~0.99), atmospheric opacity is low, and the surface-atmosphere temperature contrast is low for nighttime images, making this the most common band for deriving brightness temperatures. These factors all reduce the uncertainty in surface temperature determination [*Fergason et al.*, 2006a]. Each image is subsequently divided into framelets and the minimum, maximum and average temperatures of each framelet are stored in a database.

[14] We used a thermal model developed by H. H. Kieffer (Thermal models for analysis of Mars infrared mapping, manuscript in preparation) to derive thermal inertia values from THEMIS temperature data in addition to several other observational parameters. Mars Orbiter Laser Altimeter (MOLA) elevation data and TES Lambert albedo data with a gridded spatial sampling of 2 pixels per degree were related to THEMIS framelets by the center latitude and longitude. Two pixel per degree maps were utilized because the pixel size is nearly an equivalent in size as the coverage of a single THEMIS framelet. Other image parameters, including local solar time, solar longitude ($L_s$) for each framelet, and latitude, were also utilized in the model. The 9 $\mu$m atmospheric dust opacity was assumed to be 0.1 at the global datum for this study because, for most of the year, the infrared 9 $\mu$m dust opacity is approximately 0.1 [*Smith et al.*, 2003] and small deviations (±0.1) have less than a 3% effect on the calculated thermal inertia values [e.g., *Fergason et al.*, 2006a]. Additionally, we have not included data from the dustiest seasons and times when global and regional dust storms were active on Mars. This 9 $\mu$m dust opacity was then scaled to visible broadband opacity using a visible/9 $\mu$m extinction opacity ratio of 2.0 [*Clancy et al.*, 1995] and estimated atmospheric pressure at the surface using MOLA elevation data, assuming that dust is well mixed in the lower atmosphere.

[15] Temperature data were used to calculate thermal inertia values on a framelet basis using the thermal model. In this application of the thermal model, a lookup table of modeled surface kinetic temperatures is calculated for a variety of thermal inertias with the given parameters (latitude, solar longitude, local solar time, albedo, elevation, and atmospheric dust opacity). Thermal inertia values are then interpolated using the measured THEMIS minimum, maximum, and average estimated surface temperatures for each framelet and the calculated lookup table. After the calculation of thermal inertia values for every nighttime THEMIS temperature image (up to Mars Odyssey orbit ~25,000), the values were stored in a database, along with image and framelet observations and other derived parameters.

[16] The lookup table from which the derivation algorithm calculates thermal inertia values was limited from 0 to 2000 J $m^{-2}$ $K^{-1}$ $s^{-1/2}$. The difference between maximum temperature of the image and the temperature derived from the upper limit thermal inertia was stored in a database. This delta temperature information allowed for a more quantitative examination of images that exceeded the maximum thermal inertia of the lookup table. These delta temperatures were also used to help identify physically unrealistic data. For example, images with extreme delta temperature values (e.g., >20 K, corresponding to >6000 J $m^{-2}$ $K^{-1}$ $s^{-1/2}$) were excluded.

### 2.2. Quality Control Measures and Data Assessment

[17] In order to assure the use of well-calibrated and scientifically useful data, many constraints were placed on the data used in this work. For example, images where the time between the end of image acquisition and the collection of calibration data exceeded 150 s were omitted, because the longer this time is, the larger the uncertainty in the calibrated data due to focal plane temperature drift. Images with oversaturated or undersaturated pixels were also rejected, as these pixels can introduce undesirable image artifacts, thus influencing the overall image calibration.

#### 2.2.1. Comparison to TES Data

[18] A comparison to TES atmospheric temperature data was made to help validate the calibration of THEMIS data and the derivation of thermal inertia values and was subsequently used to further exclude THEMIS data. By comparing TES average radiance and the THEMIS average framelet radiance at 14.8 $\mu$m, we can compare the atmospheric temperature, which does not show significant variation from year to year outside of periods of high dust opacity [*Smith et al.*, 2003]. These data are compared using TES data acquired at the same $L_s$ but not necessarily from the same Mars year. Additionally, the spatial variations in atmospheric temperatures are significantly lower resolution than the size of an entire THEMIS framelet [e.g., *Smith et al.*, 2001, 2003]

providing a reasonable quality control measure for average framelet THEMIS data. The difference between TES average atmospheric radiance with a spatial sampling of 2 pixels per degree (convolved with the THEMIS band 10 spectral response function) and THEMIS band 10 average framelet radiance, was limited to less than $\pm 2 \times 10^{-5}$ W m$^{-2}$ sr$^{-1}$ $\mu$m$^{-1}$. This limit was imposed on THEMIS data because the radiance difference between two high thermal inertia values (e.g., 1200 J m$^{-2}$ K$^{-1}$ s$^{-1/2}$ and 1400 J m$^{-2}$ K$^{-1}$ s$^{-1/2}$) is expected to be $\sim 2 \times 10^{-6}$ W m$^{-2}$ sr$^{-1}$ $\mu$m$^{-1}$. A difference of this magnitude would still allow for the identification of high thermal inertia surfaces.

[19] THEMIS images in which the difference in average framelet thermal inertia values from the corresponding TES 2 ppd thermal inertia values differ by more than $\pm 220$ J m$^{-2}$ K$^{-1}$ s$^{-1/2}$ were also excluded because a difference of this magnitude would call into question the accuracy of either data set. This additional level of quality control is largely redundant with the band 10 comparison described above. The multiple layers of quality criteria ensure that the false identification of bedrock surfaces are exceedingly rare.

#### 2.2.2. Exclusion of Unrealistic and Nonphysical Values

[20] Additional quality control measures based on unrealistic or nonphysical derived thermal inertia values or spatial distributions were also applied to the data. Framelets with an average or minimum thermal inertia values of 0 J m$^{-2}$ K$^{-1}$ s$^{-1/2}$ or 2000 J m$^{-2}$ K$^{-1}$ s$^{-1/2}$ and framelets with maximum or average thermal inertia values of 0 J m$^{-2}$ K$^{-1}$ s$^{-1/2}$ were not used in this study. These erroneous values may be derived from issues such as unexpected atmospheric conditions, saturated pixels, or unrealistic surface temperatures. The final quality control check was based on visual examination of the images for image artifacts. These artifacts include features such as a single column of pixels with anomalously high values running down the length of the image.

#### 2.2.3. Confirmation and Classification of High Thermal Inertia Surfaces

[21] Each image that passed the previous quality control checks and contained one or more pixels with a value >1200 J m$^{-2}$ K$^{-1}$ s$^{-1/2}$ was individually examined to assess the morphology associated with the occurrence of the high thermal inertia surface.

[22] After the confirmation of a high thermal inertia surface (>1200 J m$^{-2}$ K$^{-1}$ s$^{-1/2}$), several image properties were recorded, including the ID number, framelet ID, and related morphologies (e.g., valley and crater walls, crater floors and plains), from both nighttime and daytime THEMIS infrared data, in addition to feature associations and textures. These properties were subsequently related to other observation parameters, such as latitude, longitude, elevation and albedo, to create a global distribution map for identified high thermal inertia surfaces (Figure 1).

### 2.3. Uncertainties and Sensitivity

[23] The calculated thermal inertia values depend on many parameters (e.g., albedo, slopes, atmospheric dust opacity) and their associated uncertainties result in the overall compounded uncertainty in the calculated thermal inertia. Uncertainties are also associated with the estimated surface temperatures, which are the largest contributor to the uncertainty in thermal inertia and may vary by up to $\sim$2.9 K between images [*Fergason et al.*, 2006a]. Figure 2 illustrates the effect on thermal inertia of a 2.9 K temperature difference. For example, at $\sim$220 K ($\sim$1000 J m$^{-2}$ K$^{-1}$ s$^{-1/2}$) and higher, a 2.9 K temperature difference yields a thermal inertia difference of $>\sim$200 J m$^{-2}$ K$^{-1}$ s$^{-1/2}$. Additionally for slightly higher temperatures (e.g., >230 K), the uncertainty in thermal inertia could be as high as 1000–1500 J m$^{-2}$ K$^{-1}$ s$^{-1/2}$, making interpretations even more difficult. *Fergason et al.* [2006a] discuss many parameters in addition to calibration inaccuracies that may contribute to uncertainty associated with thermal inertia, including the effects of albedo (0.03, 6% uncertainty), elevation (100 m, 0.5–1% uncertainty), slopes (1°, 3% uncertainty), variable emissivity (1.2 K, 6%) and atmospheric dust opacity (0.1, 3% uncertainty).

[24] It is difficult to make quantitative comparisons between two high thermal inertia surfaces because above thermal inertia values of $\sim$1200 J m$^{-2}$ K$^{-1}$ s$^{-1/2}$, an incremental difference in thermal inertia yields a proportionally smaller difference in thermal inertia. Thus, there is little meaningful difference between a 1200 J m$^{-2}$ K$^{-1}$ s$^{-1/2}$ and a 2000 J m$^{-2}$ K$^{-1}$ s$^{-1/2}$ surface, which has an associated temperature difference of 2.9 K (Figure 2). However, Figure 2 illustrates that while it may be difficult to distinguish the subtle details of surfaces with very high thermal inertia values, one can accurately/reliably distinguish a high thermal inertia surface from a low or moderate thermal inertia surface. The precision and accuracy of the method used here is more than sufficient to provide the means to identify and classify these high thermal inertia surfaces.

## 3. Results

[25] Nearly 450,000 THEMIS framelets pass the quality control measures and have been considered in this study, covering $\sim$73% of the planet from latitudes between 75°S and 75°N and accounting for overlap. Of these, only 960 framelets were identified as containing bedrock. In some cases, these framelets overlap and therefore the number of identified framelets is an upper limit of the number of unique surfaces identified. Determining the exact area that these locations cover on Mars is not straightforward, as only one pixel in the framelet is required to positively identify bedrock. However, an estimate can be made if we take the typical number of pixels containing exposed bedrock in a framelet ($\sim$300 pixels, corresponding to $\sim$0.5% of the 76,800 pixels in a framelet), the corresponding surface area of bedrock on Mars is less than $\sim$3500 km$^2$, assuming there is no framelet overlap. Even though this number is likely a significant overestimate, the total surface of exposures of bedrock on Mars represents $\ll$1% of the total surface area.

[26] Figure 3 is a histogram of all valid THEMIS framelets (5° latitude bins) with identified instances of bedrock normalized to THEMIS coverage versus latitude. These histograms indicate that bedrock exposures are not present at high latitudes despite ample coverage at these latitudes. The Martian surface is not completely covered in high-quality THEMIS nighttime temperature images and it is possible that additional instances of high inertia surfaces exist. However, coverage of the planet's surface is extensive enough to have a high degree of confidence in the trends identified.

[27] High thermal inertia materials are primarily associated with three types of morphologies: (1) valley and crater walls

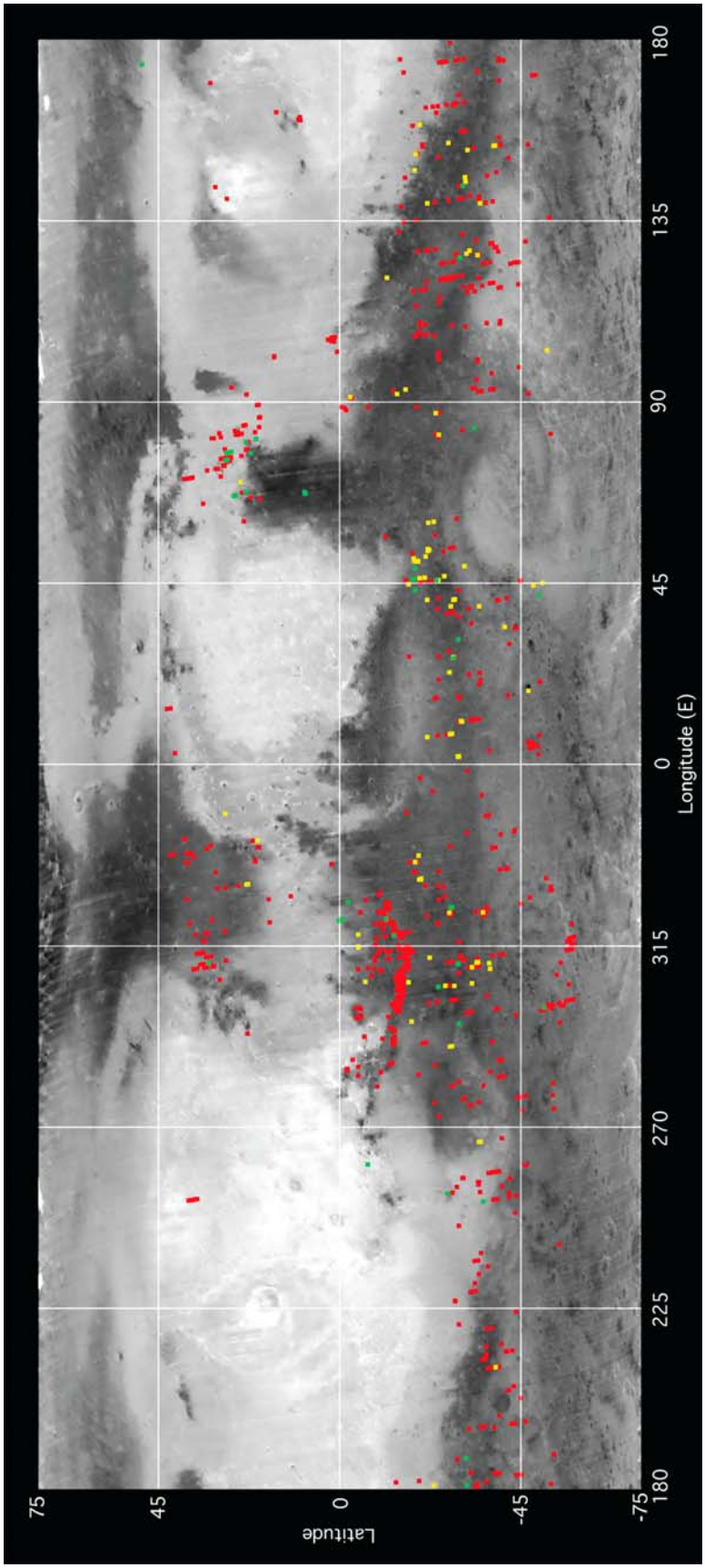


**Figure 1.** Distribution of identified bedrock morphologies between 75°S and 75°N overlain on a TES Lambert albedo global map of Mars. In all, 960 instances have been identified using THEMIS high-resolution thermal inertia. Red corresponds to the valley and crater wall surfaces, yellow corresponds to the crater floor surfaces, and green corresponds to the intercrater surfaces. Most of these instances occur in low-albedo regions and indicate that these surfaces are generally exposed where dust content is low. Additionally, there are few instances of high thermal inertia surfaces observed poleward of 45°N and 58°S, which may indicate enhanced regolith formation due to an active freeze-thaw process.

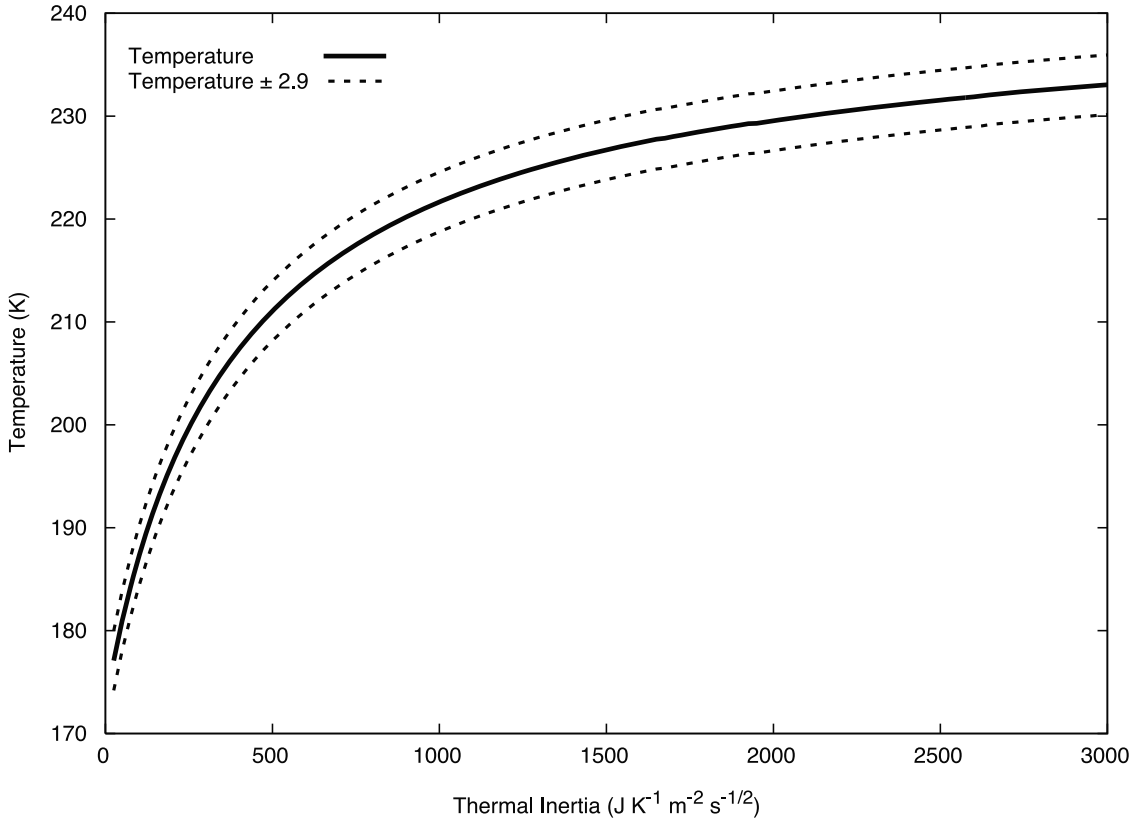


**Figure 2.** Three curves illustrate the decreasing sensitivity of thermal inertia at higher values for a typical range of THEMIS temperature uncertainty (±2.9 K). Other parameters for model curves are fixed, where solar longitude is 270°, local solar time is 0440 (similar to that of the Mars Odyssey orbit), the latitude is 21.2°S, the elevation is 500 m, and the albedo is 0.10. These values are representative of what is typically observed for the southern highlands where most of the high thermal inertia surfaces are identified.

with steep slopes (821 instances); (2) crater floor surfaces (92 instances); and (3) intercrater surfaces not related to any major topographic feature and commonly showing wind scoured morphologies, such as a rough and pitted textures (47 instances).

### 3.1. Global Bedrock Distribution

[28] We created a map that shows the distribution of all three types of high thermal inertia surfaces from 75°S to 75°N (Figure 1). Clear regional groupings are evident with all instances of high thermal inertia surfaces. Most occurrences are located in the heavily cratered southern highlands and Valles Marineris; there are few exposures in the northern lowlands and in regions with an albedo greater than 0.18, such as the Tharsis, Arabia, and Elysium regions (Figures 1 and 4a).

[29] In addition to being relatively dust-free, the southern highlands generally contain moderate thermal inertia values and locations like Valles Marineris are associated with some of the highest thermal inertias on the planet at the lower spatial scale of the TES data [*Mellon et al.*, 2000; *Putzig et al.*, 2005]. This contrasts with the equatorial dust-mantled regions with some of the lowest thermal inertias on the planet [*Mellon et al.*, 2000; *Putzig et al.*, 2005]. The equatorial dust-mantled regions and the southern highland regions observed in TES data appear to correlate with the higher-resolution observations presented here. The dust-mantled regions exhibit few bedrock exposures while the vast majority of bedrock instances are located in the cratered southern highlands, which have typically elevated THEMIS average framelet thermal inertia values (e.g., >300 J $m^{-2}$ $K^{-1}$ $s^{-1/2}$ (Figure 4b)).

[30] Additionally, most high thermal inertia surfaces occur in areas with a high dust cover index (DCI) value (typically >0.95 [*Ruff and Christensen*, 2002]) that indicates a relatively dust-free surface (Figure 4c). This is not unexpected as small amounts (less dust cover) would result in lower values of thermal inertia. However, high thermal inertia surfaces do not always occur in low-albedo, dust-free regions. Figure 4a shows that a significant fraction of bedrock instances occur in moderate to high-albedo regions (>0.20). Most of these instances correspond to the moderate-albedo area to the north of Syrtis Major near Nilosyrtis Mensae and near the rim of Isidis basin. Bedrock associated with the highest-albedo surfaces (>∼0.27) corresponds to a few instances identified in dusty, low thermal inertia areas near the Tharsis and Elysium volcanic provinces. These outliers in the moderate- to high-albedo regions are generally consistent with a relatively thin coating of dust (likely <∼5 $\mu$m [e.g., *Mellon et al.*, 2008; *Putzig and Mellon*, 2007b]) and not a complete mantling of the surface. However, in most cases bedrock exposures are associated with relatively lower albedo areas within the larger high-albedo regions.

[31] The distribution of bedrock on Mars appears to be latitudinally limited, with only one instance occurring at

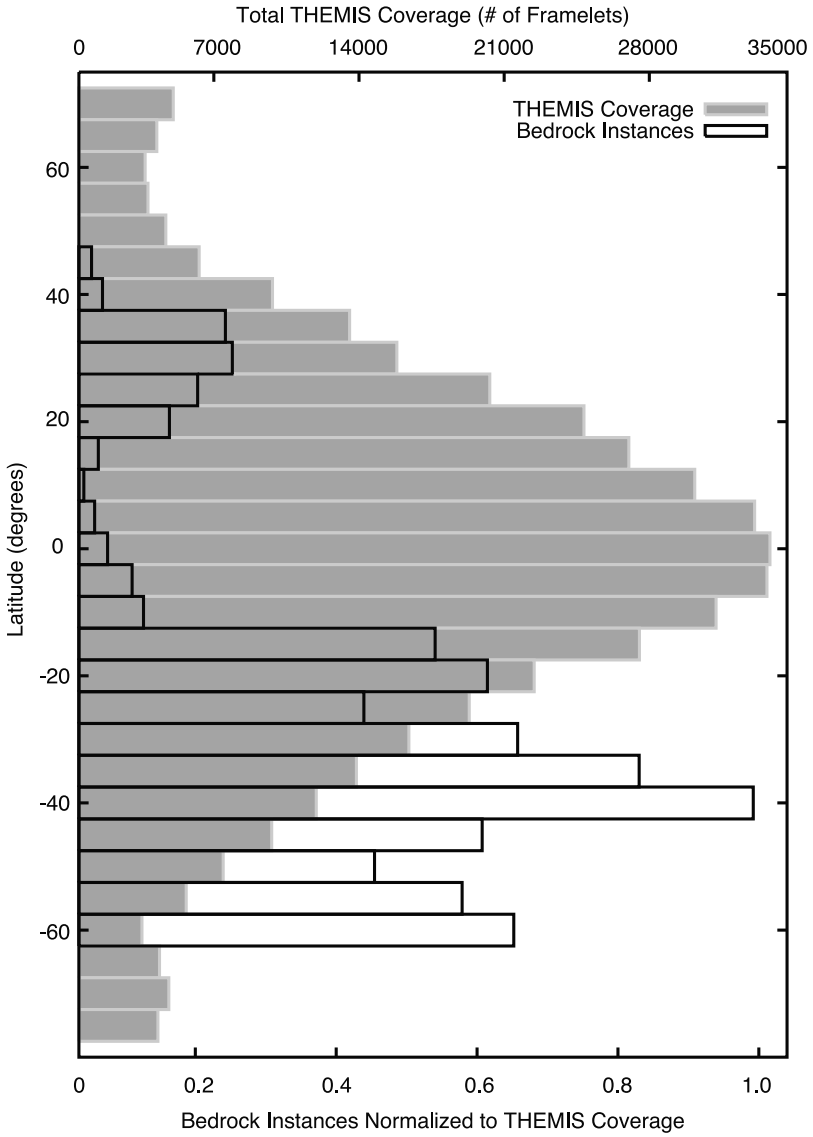


**Figure 3.** Histograms of total THEMIS coverage (solid gray and the top scale) and bedrock instances normalized to THEMIS coverage and subsequently normalized to one (black outline and the bottom scale) versus latitude. Only potentially valid THEMIS framelets have been included in this histogram (~450,000), which illustrates that the high-latitude regions are well covered by valid data meeting the same criteria for instances of bedrock (e.g., shutter closing time <150 s, TES-THEMIS radiance difference $<2 \times 10^{-5}$ W $m^{-2}$ $sr^{-1}$, TES-THEMIS thermal inertia difference <200 J $m^{-2}$ $K^{-1}$ $s^{-1/2}$, average and minimum THEMIS thermal inertia <2000 J $m^{-2}$ $K^{-1}$ $s^{-1/2}$ and >0 J $m^{-2}$ $K^{-1}$ $s^{-1/2}$, solar incidence angle >95°, and a local solar time of >0200 and <0630). Bedrock instances have been normalized to THEMIS coverage to reduce effects of sampling bias and illustrate that the bulk of the identified surfaces occur in the southern hemisphere.

**Figure 4.** (a) Histogram of high thermal inertia surface frequency (thermal inertia values >1200 J $m^{-2}$ $K^{-1}$ $s^{-1/2}$ normalized for the frequency of TES Lambert albedo for THEMIS framelets) versus TES Lambert albedo. Most instances of bedrock occur in regions with low albedo, typically <0.18. However, there are many instances in moderately high albedo areas (>0.20). (b) Histogram of high thermal inertia surface frequency (thermal inertias >1200 J $m^{-2}$ $K^{-1}$ $s^{-1/2}$ normalized for the frequency of THEMIS average thermal inertia) versus THEMIS average thermal inertia. Most instances occur in regions with moderately high THEMIS thermal inertia (>400 J $m^{-2}$ $K^{-1}$ $s^{-1/2}$). (c) Histogram of high thermal inertia surface frequency (thermal inertia values >1200 J $m^{-2}$ $K^{-1}$ $s^{-1/2}$ normalized for the frequency of TES dust cover index for THEMIS framelets) versus TES dust cover index. Most bedrock instances occur in regions with a low dust cover (DCI > 0.95).

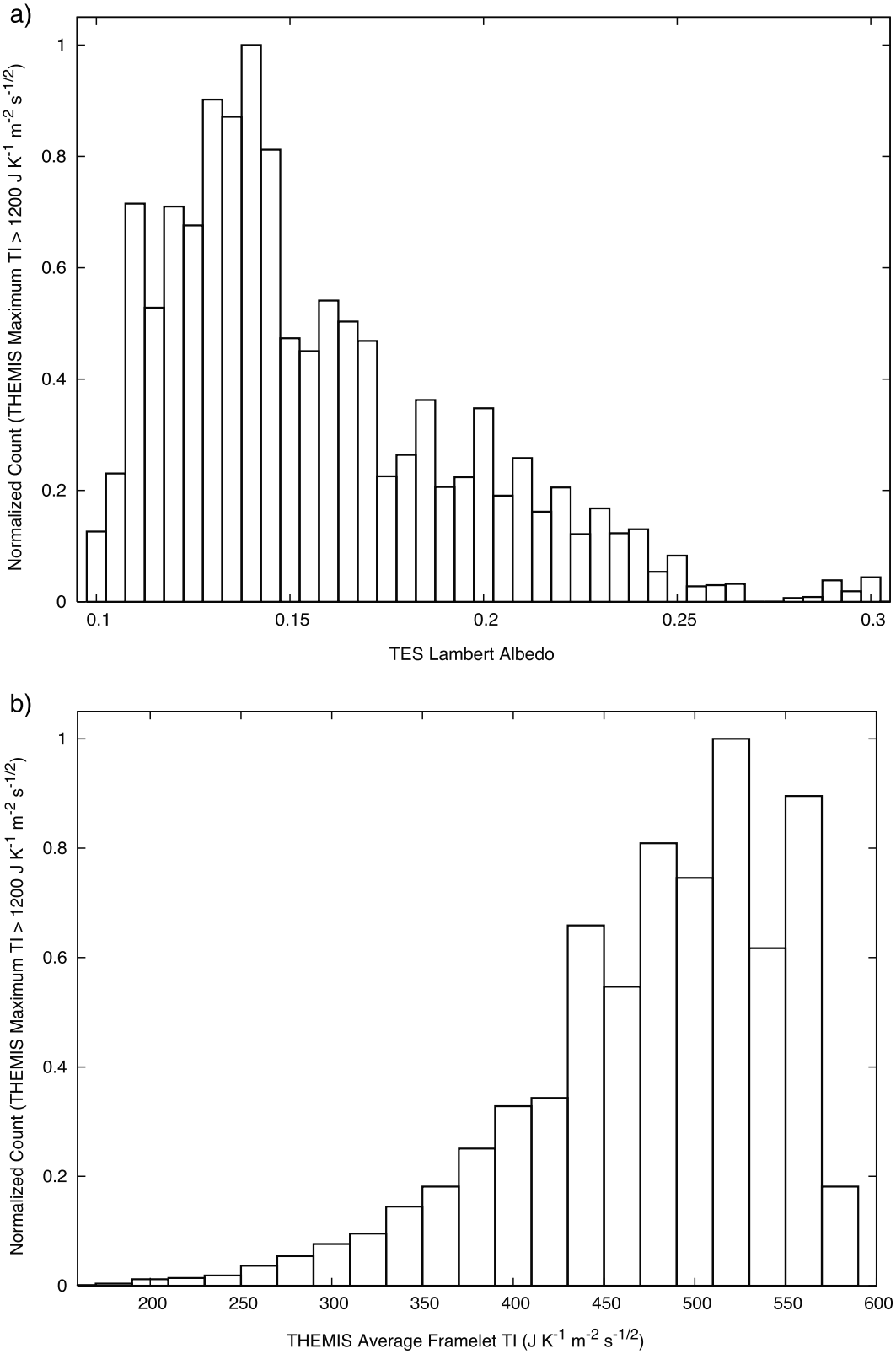
a)
Normalized Count (THEMIS Maximum TI > 1200 J K-1 m-2 s-1/2)
0
0.2
0.4
0.6
0.8
1
0.1
0.15
0.2
0.25
0.3
TES Lambert Albedo
b)
Normalized Count (THEMIS Maximum TI > 1200 J K-1 m-2 s-1/2)
0
0.2
0.4
0.6
0.8
1
200
250
300
350
400
450
500
550
600
THEMIS Average Framelet TI (J K-1 m-2 s-1/2)

**Figure 4**

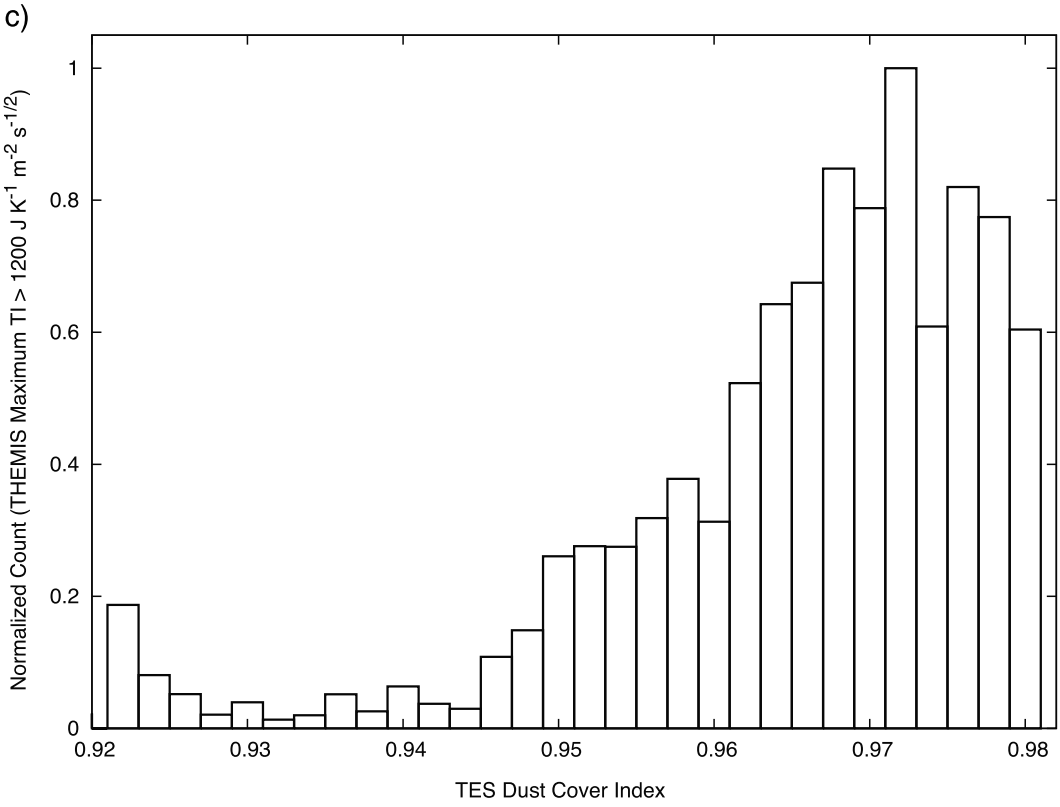


**Figure 4.** (continued)

latitudes northward of 45°N and no instances occurring southward of ~58°S (Figure 3). This is despite the presence of regions at high latitudes with TES thermal inertia values (>~220 J $m^{-2}$ $K^{-1}$ $s^{-1/2}$), DCI (>~0.95), and TES albedo (<~0.18) consistent with a majority of the bedrock instances identified globally.

### 3.2. Valley and Crater Wall Bedrock Exposures

[32] High thermal inertia surfaces located on valley and crater walls are the most common type of bedrock exposure observed. This morphology is mainly concentrated in low-albedo regions (typically <~0.15) within the southern highlands. There are a variety of morphologic features associated with this surface type, ranging from steep slopes in Valles Marineris (Figure 5) to the walls and rims of craters, small hills, and knobby terrain (e.g., chaos terrain). When this surface is found within craters, it is often times associated with largely unmodified craters of various sizes. This surface type has thermal inertia values that often reach the maximum of the lookup table (2000 J $m^{-2}$ $K^{-1}$ $s^{-1/2}$) and it is likely that even higher thermal inertia values are present. Spur and gully morphology is commonly associated with this surface type (Figure 5). Bedrock is typically exposed along a ridge or spur and lower thermal inertia mantling materials infill topographic lows or gullies between spurs.

[33] A THEMIS visible image (Figure 5b) displays the typical spur and gully morphology associated with this surface, where the bedrock is concentrated near the tops of ridges. Associated high-resolution Mars Orbiter Camera (MOC) [*Malin et al.*, 1998] and HiRISE imagery (Figures 5c and 5d) further emphasizes the morphologies with which these high thermal inertia surfaces are commonly associated. Spurs and ridges are unmantled, have a rough texture, and numerous large boulders are clearly visible. Gullies generally exhibit a smooth and mantled morphology, often with aeolian bed forms.

### 3.3. Crater Floor Bedrock Exposures

[34] Occurrences of high thermal inertia surfaces within crater floors (Figure 6) are less common than within valley and crater walls. The material in the floors of these craters has a much higher thermal inertia than the walls of these craters. Craters with bedrock exposed on their floors are commonly modified; they typically lack a central peak, have shallow sloped walls, have little to no visible ejecta material, and occasionally gullies and subsequent impact craters are present. The average crater diameter is ~52 km (median diameter of ~49 km) with a standard deviation of 26 km; all craters of this type have diameters between 18.5 and 179 km. The distribution of this surface type is mainly concentrated in low-albedo surfaces within the southern highlands. However, high thermal inertia crater floor surfaces occasionally occur in higher-albedo areas, specifically in Chryse and Acidalia Planitia.

[35] The floors of these craters commonly have both high and low thermal inertia areas. High thermal inertia surfaces observed in THEMIS and MOC visible images (Figures 6b and 6c) are generally rough and pitted and are commonly elevated above the surrounding terrain, indicating that they are more resistant to erosion than other material in the crater bottoms. Relatively higher albedo features in Figures 6b and 6c correlate with the high thermal inertia material observed in Figure 6a. Lower thermal inertia features (blue and yellow tones in Figure 6a corresponding to thermal inertia values of ~180 J $m^{-2}$ $K^{-1}$ $s^{-1/2}$ to 600 J $m^{-2}$ $K^{-1}$ $s^{-1/2}$) are generally

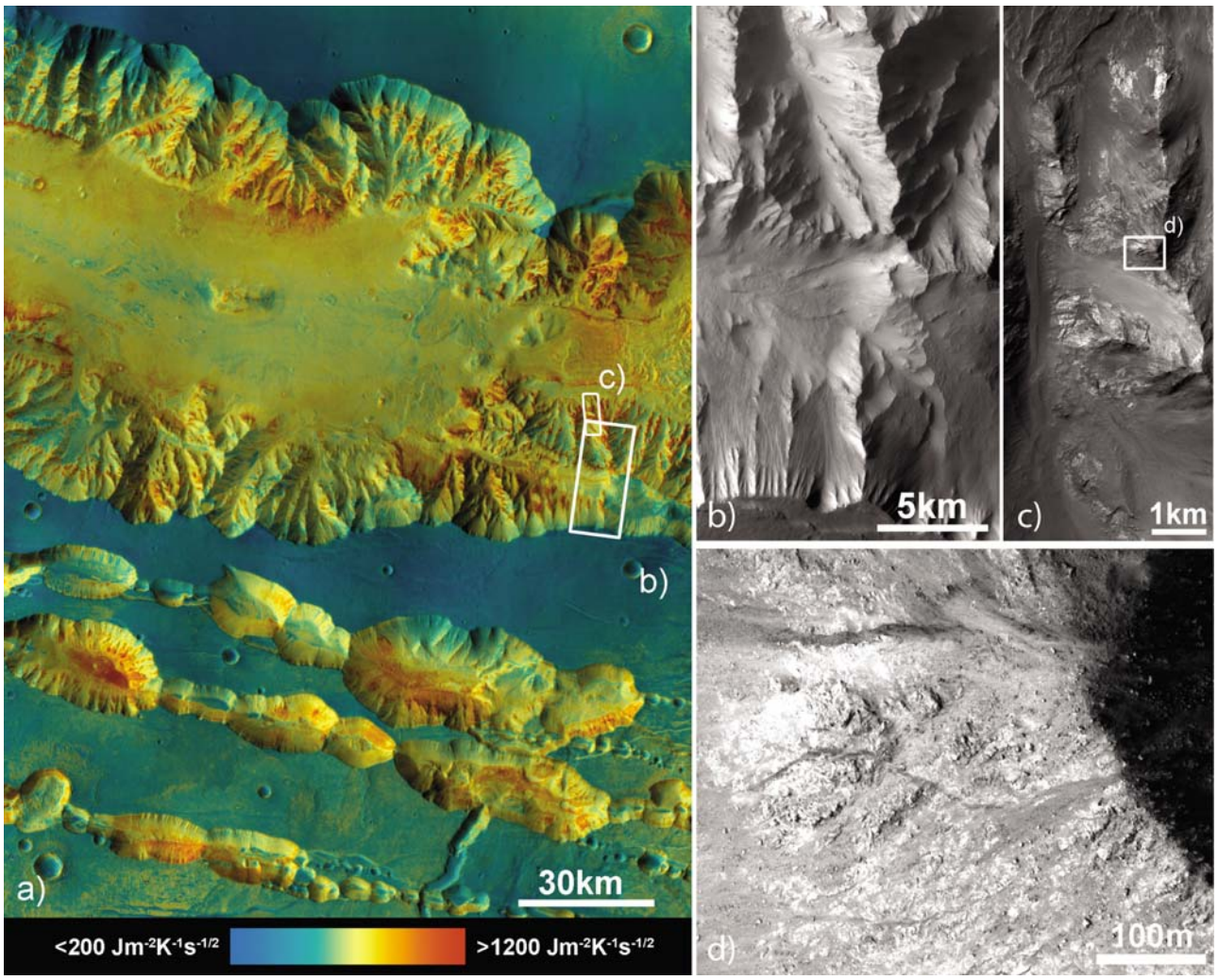


**Figure 5.** (a) A colorized THEMIS nighttime temperature mosaic over a THEMIS daytime temperature mosaic which depicts high thermal inertia valley walls, centered at −13.75°N, 299.25°E. The blues in the image correspond to thermal inertia values of less than 200 J $m^{-2}$ $K^{-1}$ $s^{-1/2}$, and the reds in the image correspond to thermal inertia values of at least 1200 J $m^{-2}$ $K^{-1}$ $s^{-1/2}$. (b) THEMIS visible image (V10900002) illustrates the spur and gully nature of many of the instances of the valley wall high thermal inertia surfaces. High thermal inertia values are commonly associated with spurs, while lower thermal inertia material infills the gullies. (c) MOC high-resolution image (E2101368) further illustrates this type of surface where bedrock appears to be exposed. (d) HiRISE image (PSP_003513_1665) is located on the top of one of the spurs and shows in-place rock and boulders on the surface likely derived from that rock. Additionally, there is lower-albedo material, which appears to be sediment eroded from the rock outcrops.

located in topographic lows and may be representative of areas infilled with aeolian material as evidenced by bed forms (Figure 6c).

[36] In many instances, HiRISE images (Figure 6d) reveal that these high thermal inertia surfaces are heavily fractured. These fractures are apparently randomly oriented. Lower-albedo material that is likely aeolian in origin fills many of these fractures. Larger depressions also appear to be filled by similar material and commonly exhibit aeolian bed forms in high-resolution imagery. However, because the spatial sampling of the THEMIS data is ∼100 m and the HiRISE data has a spatial sampling of ∼0.25 m, these bed forms (typically <5 m) cannot be resolved in the THEMIS thermal inertia data, and thus we cannot interpret an equivalent grain size, but these bed forms have been shown to occur within a restricted grain-size range (likely <1 mm) [*Presley and Christensen*, 1997a]. No channels or other fluvial features are observed in association with this surface type, and therefore the erosional agent most likely associated with this surface is wind.

### 3.4. Intercrater Surface Bedrock Exposures

[37] The intercrater high thermal inertia surface type has been identified on the basis of its lack of correlation with steep slopes, crater walls or crater floors. It is the least common high thermal inertia surface type and is generally found in the intercrater plains, in low-albedo regions (<∼0.15) within the southern hemisphere. It is found in other regions and a cluster of this surface type is observed in a moderate-albedo region (>0.20) to the north of Syrtis Major. Figure 7 illustrates a typical example of surface textures

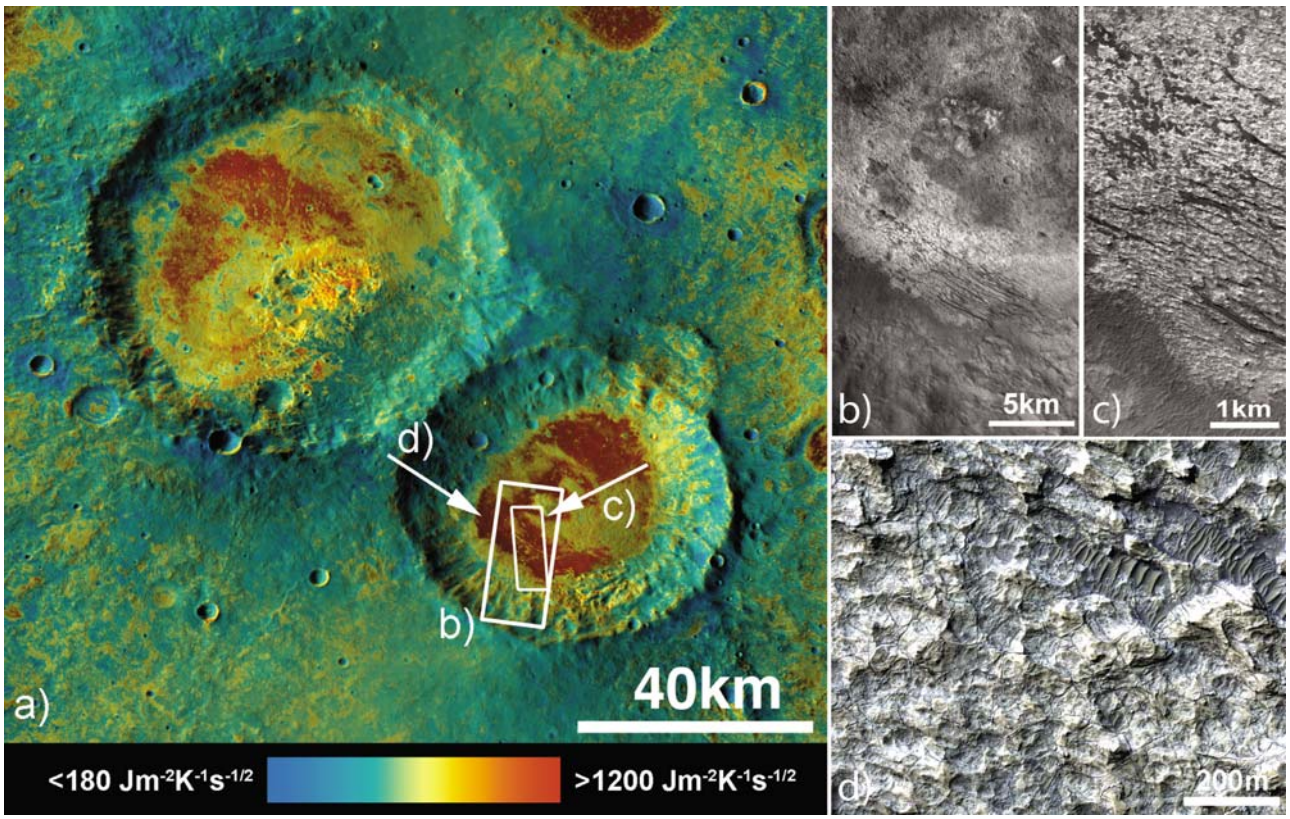


**Figure 6.** (a) A colorized THEMIS nighttime temperature mosaic over a THEMIS daytime temperature mosaic which depicts a crater with material of high thermal inertia on its floor, centered at −25.25°N, 47.5°E. The blues in the image correspond to thermal inertia values of less than 180 J m$^{-2}$ K$^{-1}$ s$^{-1/2}$, and the reds in the image correspond to thermal inertia values of at least 1200 J m$^{-2}$ K$^{-1}$ s$^{-1/2}$. (b) THEMIS visible image (V15651003) illustrates the rough, pitted, and relatively higher albedo of the high thermal inertia material. In general the highest thermal inertia values are associated with the light-toned, heavily pitted material. (c) MOC high-resolution image (E1801469) further illustrates the pitted textures associated with these high thermal inertia surfaces. Additionally, lower-albedo material is observed on the high thermal inertia, light-toned material, which is likely aeolian material as evidenced by observed dune forms. (d) Color (infrared, blue, and red channels) HiRISE image (PSP_007689_1540) is an example of high thermal inertia material found in crater bottoms. In this case, the yellowish tones are associated with high thermal inertia material. This image also illustrates the highly fractured and pitted terrain often associated with these craters.

associated with this surface type. These units are not generally associated with any lowstanding or highstanding topographic feature in the intercrater highlands, but they may be associated with features such as channel floors or the ejecta of large craters.

[38] The intercrater surface type exhibits characteristics similar to the crater floor high thermal inertia surface type, such as a rough and textured surfaces apparent in THEMIS visible and MOC narrow angle images (Figure 7). HiRISE imagery of the area shows a rocky and pitted texture on this surface with aeolian ripples in local depressions (Figure 7d). As is the case with the crater floor surfaces, these high thermal inertia surfaces are commonly the highest stratigraphic unit observed in the immediate area, excluding mantling material. In addition, they are often cut by fractures or channels indicating that fluvial, tectonic, and aeolian processes may be eroding these surfaces more slowly than the surrounding lower thermal inertia material. However, *Rogers et al.* [2009] have shown that this surface type can be both topographically higher and lower than other materials. In the case shown in Figure 7, the high thermal inertia surface is topographically higher than the lower thermal inertia areas. This observation and the difference in albedo present in visible images indicates that, at least in this case, it is possible that this high thermal inertia surface is a semicontinuous layer that has been preferentially eroded in some locations, revealing underlying lower thermal inertia layers.

## 4. Discussion

### 4.1. Global Distribution

[39] The abundance of high thermal inertia surface instances in the cratered southern highlands (Figures 1 and 4) corresponds well with the moderate thermal inertia regions described by *Putzig et al.* [2005], *Mellon et al.* [2000] and *Christensen* [1982]. High thermal inertia surfaces are not commonly found in other midlatitude and equatorial regions,

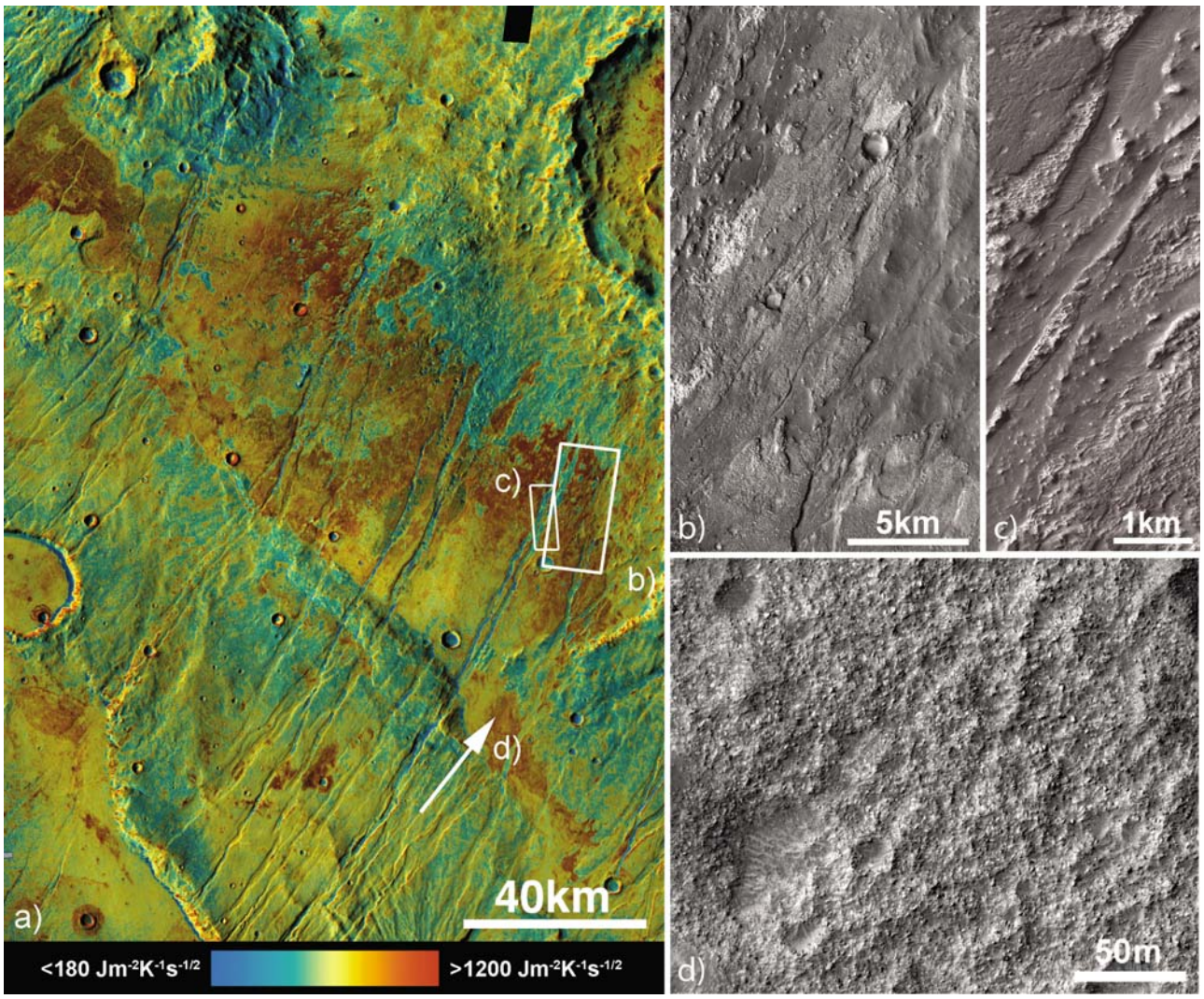


**Figure 7.** (a) A colorized THEMIS nighttime temperature mosaic over a THEMIS daytime temperature mosaic which depicts a high thermal inertia intercrater bedrock unit, centered at −34.75°N, 250.5°E. The blues in the image correspond to thermal inertia values of less than 180 J $m^{-2}$ $K^{-1}$ $s^{-1/2}$, and the reds in the image correspond to thermal inertia values of at least 1200 J $m^{-2}$ $K^{-1}$ $s^{-1/2}$. (b) THEMIS visible image (V07719004) illustrates the rough pitted texture of many of the instances of the intercrater high thermal inertia surfaces. High thermal inertia values are commonly associated with rough pitted terrain and are generally elevated above the surrounding country material. (c) MOC high-resolution image (R1801370) also illustrates this rough and pitted texture. High thermal inertia values are commonly associated with the lower-albedo material observed in the top left of this image. Additionally, it appears in this location there may be more than one layer of this material present. This material also seems to be cut by channels, which now are being infilled with aeolian material as evidenced by the dune forms observed in this image. (d) HiRISE image (PSP_006785_1440) of the high thermal inertia intercrater surface. In this case, the high thermal inertia material appears as rocky outcrops with some boulders likely derived from the in-place rock, as well as some aeolian material which infills depressions in the high thermal inertia surface.

presumably because of the large degree of dust mantling in these areas (Figures 4a and 4c).

#### 4.1.1. Anomalous High Thermal Inertia Surface in High-Albedo Regions

[40] A wide range of latitudes on Mars have high thermal inertia (>∼350 J $m^{-2}$ $K^{-1}$ $s^{-1/2}$), high DCI (>∼0.95), and low TES albedo (<∼0.18), but bedrock is highly latitudinally limited. Even though the global coverage included ±75° latitudes, we identified only one instance of high thermal inertia surfaces north of 45°N and no instances south of −58°N. This observation suggests that a geologic process unique to the high-latitude regions of Mars may be either obscuring or destroying underlying rock.

[41] There are several anomalous clusters and individual instances of high thermal inertia surfaces that do not follow the trends identified in Figure 4 (e.g., areas with elevated albedo or especially low average thermal inertia values) and do not follow the typical latitudinal distribution. The feature

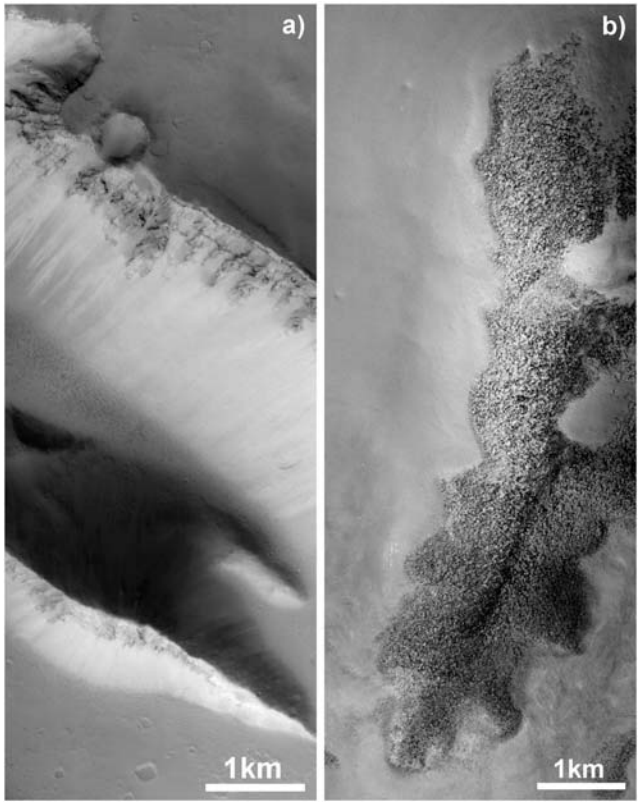


**Figure 8.** (a) MOC image (E1002786, centered at 140.5°E, 27.5°N) of an anomalous valley and crater wall surface to the northwest of Elysium. This surface (top part of image) is located on a steep wall of a surface crack where some spurs are observed. These lighter-toned spurs with layering are associated with the high thermal inertia surface. Additionally, some slope streaks are observed, indicating recent activity where dust moved downhill obscuring darker-toned material. (b) MOC image (R1900477, centered at 173.8°E, 49.2°N) of an anomalous intercrater surface to the north of Propontis. This instance is located significantly higher than any other intercrater surface and is the northernmost instance of bedrock observed in this study. The high thermal inertia material is associated with the lower-albedo rough surface, which appears to be embayed by mantling material. The lower-albedo material is also associated with a topographic high.

shown in Figure 8a is a valley and crater wall surface type located in a dusty area in the northwest of Elysium (140.5°E, 27.5°N). This surface is located on a steep wall of a surface fracture or rift. Overall, the terrain has a smooth and mantled appearance, but there are several locations, especially at the steepest parts of the walls, where lighter-toned spurs with apparent layering are observed. This roughly horizontal layering may be lava flows from the Elysium volcanic province that have since been exposed in the walls of this fracture. Valley and crater wall surfaces in the large volcanic provinces may be locations where slopes are steep enough to prevent mantling and reveal the bedrock underlying the otherwise dust-mantled terrain.

[42] In addition, a large grouping of a variety of bedrock types is observed to the north of Syrtis Major in a moderate-albedo region (>0.2). It is possible that insufficient dust has fallen to obscure the bedrock signature in the thermal inertia data as this area is expected to have lower dust fall rates [e.g., *Basu et al.*, 2004]. However, less than ~1 cm of dust could have fallen over the millions of years since these features formed, yet with the deposition of $\ll$1 mm of dust, these high thermal inertia surfaces would no longer be identified using the methods presented here. Alternatively, this grouping may indicate high winds in this area [e.g., *Fenton and Richardson*, 2001], which could be keeping surfaces clear of mantling material. The examples provided of anomalous high thermal inertia surfaces illustrate types of exposure mechanisms where bedrock is insufficiently mantled to mask the high thermal inertia signature.

#### 4.1.2. High-Latitude Occurrences and Periglacial Processes

[43] The formation mechanism for high latitude (>~50°) terrain with few rocky outcrops is not well constrained. Surface morphologies in higher latitudes display a mantled and generally smooth morphology with some hummocky topography at ~10–1000 m scales. The presence of abundant near surface ice through the Martian high-latitude regions [e.g., *Bandfield and Feldman*, 2008; *Feldman et al.*, 2002; *Kreslavsky et al.*, 2008; *Mitrofanov et al.*, 2002] could be accounted for by enhanced mechanical processing of near surface material associated with periglacial landscapes [*Kreslavsky et al.*, 2008]. The active layer in these permafrost terrains is subject to seasonal and daily freeze/thaw cycles [*Mellon and Jakosky*, 1995], which occurs at different intensities in different hemispheres throughout the recent Martian past [*Kreslavsky et al.*, 2008; *Mellon and Jakosky*, 1995]. Periglacial processes that cause the mechanical breakdown of regolith materials result in the lack of any steep slopes poleward of 60° latitude and the lack of steep pole-facing slopes poleward of 30° latitude [*Kreslavsky et al.*, 2008]. This breakdown could also be responsible for the distinct lack of high thermal inertia surfaces at high latitudes. Cycling of water ice through freezing and sublimation in the subsurface as well as thermal expansion and contraction breaks up near-surface material by fracturing and other related weather processes and may be forming a regionally extensive regolith at high latitudes. By repeating this cycle over many millions of years, a large amount of relatively fine particulate material could build up and bury any high thermal inertia material present at these higher latitudes.

[44] The seasonal thermal wave typically propagates decimeter to meter depths [e.g., *Armstrong et al.*, 2005; *Paige et al.*, 1994; *Titus et al.*, 2003], while the diurnal thermal wave is superposed on the seasonal wave and typically propagates millimeters to centimeters [*Kieffer et al.*, 1977; *Mellon et al.*, 2000, 2008]. As a result, it is possible to use temperature measurements taken over the course of a season to determine heterogeneity in thermophysical properties. For instance, ice-cemented soil at shallow depths causes a reduction in the overall amplitude of the seasonal temperature curve, affecting the rate of cooling in late summer and early autumn, where the surface temperature remains warmer than a surface with a deep ice layer or no layer at all [*Bandfield*, 2007]. Although nowhere exposed on the surface (except the ice caps themselves), Martian high latitudes have properties consistent with extensive high thermal inertia (2290 J $m^{-2}$ $K^{-1}$ $s^{-1/2}$) materials within a few centimeters of the surface

[*Bandfield and Feldman*, 2008; *Paige et al.*, 1994; *Putzig and Mellon*, 2007b]. The presence of permafrost precludes surface exposures of high thermal inertia materials both because of its inherent instability at the surface and periglacial processing of any other high thermal inertia materials that may be present.

[45] A north-south asymmetry in the maximum latitudinal extent is observed in the distribution of high thermal inertia surfaces (Figure 3). This asymmetry may indicate that the periglacial process that acted on the underlying rock occurred at lower latitudes in the northern hemisphere than in the southern hemisphere. With changes in obliquity and eccentricity, it is possible that the latitudinal asymmetry in observed bedrock instances could be explained by enhanced freeze/thaw action in the past [e.g., *Jakosky et al.*, 1995; *Mellon and Jakosky*, 1995]. Even under current Martian conditions, permafrost is detected near the surface to lower latitudes in the northern hemisphere ($\sim$55°N) than in the southern hemisphere ($\sim$65°S). The differential extent of the permafrost is likely a contributing factor to the asymmetry observed.

[46] The intercrater surface shown in Figure 8b at 49.2°N is located much further north than any other high thermal inertia surface and is associated with a small hill that has shallow slopes. The surface appears to be rocky with rough and pitted textures visible in MOC imagery. The smooth, mantling terrain has likely been stripped away in isolated patches by aeolian processes. It is possible that this hill was a volcanic eruptive center at some point in the past and that this terrain is the remnant flows of these events. This potential eruptive vent is in an area that exhibits many features similar to those observed in other locations that are interpreted to be rootles cones [e.g., *Bruno et al.*, 2006; *Greeley et al.*, 2000; *Lanagan et al.*, 2001].

### 4.2. Valley and Crater Wall High Thermal Inertia Surfaces

[47] Dust and other mantling materials are typically unstable on slopes of >$\sim$27° under Martian conditions [e.g., *Gerstell et al.*, 2004; *Sullivan et al.*, 2001]. Due to the steep slopes on which these high thermal inertia features commonly occur; dust, silt, and sand are not likely to accumulate, leaving the underlying bedrock exposed. Slopes significantly steeper than $\sim$27° are commonly observed throughout Valles Marineris and in many of the craters identified. However, the western end of Valles Marineris, where few bedrock instances are observed, has similar slopes to eastern end of the canyon, where many bedrock instances are observed, indicating that the slope of the surface is not the only controlling factor. Evidence for mass wasting processes, such as gullies and slumping, are also evident in many of these instances, where it is likely that a rocky, less weathered surface is exposed. Erosion associated with high-velocity winds probably also plays a large role in exposing high thermal inertia surfaces. The spur and gully morphology observed in Figure 5 may also be evidence of preferential weathering of different units, where more resistant units form cliffs and steep scarps while other less resistant units form shallower slopes [e.g., *Sullivan*, 1992]. These deposits may have a variety of potential primary formation mechanisms, including lava flows, intrusive igneous activity, or lithification of sediments.

[48] The concentration of high thermal inertia exposures decreases toward the western portion of the canyon and closer to the higher-albedo, dust mantled Tharsis region. The Tharsis low-inertia region (and other similar regions) show only five occurrences of high thermal inertia surfaces which is consistent with a high-albedo, dust covered surface [*Ruff and Christensen*, 2002]. The several instances of this surface type that do occur in high-albedo, low thermal inertia areas (Figure 8a), can likely be attributed to more recent mass wasting and erosion. It may be possible to use the results from this study to constrain the rates of dust accumulation or identify locations with recent impact and mass wasting activity. The processes occurring at these locations must be a steady state case where bedrock is not completely eroded or mantled. In these instances, the dust deposition rates, likely less than a few microns per year [e.g., *Christensen*, 1988; *Pollack et al.*, 1979], must be similar to erosion or mantling removal rates. Erosion rates noted at the Mars Exploration Rover (MER) landing sites [e.g., *Golombek et al.*, 2006] suggest that erosional processes on Mars are significantly slower (0.03 – 10 nm/year) at these locations. However, these erosion rates are reported for sulfates and are likely significantly slower than the rate at which the removal of mantling material occurs. Processes occurring at bedrock locations must have either lower than predicted dust deposition or higher mantling material removal rates than the erosion rates observed at the MER landing sites for bedrock to remain exposed.

[49] This surface type, while the most common of the three identified, is still rare. There are many instances of steep slopes (>$\sim$27°) on Mars, even in low-albedo, relatively dust-free areas, where these types of exposures would be expected, yet they are not observed. For instance, the areas south of both Syrtis Major and Meridiani Planum meet these criteria, yet exhibit few to no instances of bedrock. This lack of widespread exposures may indicate global-scale crustal processing, which either obscures or destroys most bedrock on Mars. The high thermal inertia locations that are observed may have undergone less processing than the rest of the planet. However, another possibility for the exposure of high thermal inertia surfaces is that the downslope motion associated with mass-wasting events is occurring at a higher rate than the rate of mantling or there is sufficient wind to keep the surfaces free of these materials.

### 4.3. Crater Floor Surfaces

[50] The crater floor surface type has a morphology (fractured, rough and pitted surfaces, size threshold) that suggests the presence of impact melting or impact associated volcanism as the process responsible for the high thermal inertia materials. Craters with impact melt and impact related volcanism have been identified on the Moon [e.g., *Schultz*, 1976; *Smrekar and Pieters*, 1985; *Wilhelms et al.*, 1987] and have similar morphologic characteristics to those identified in this study. For example, these craters on the Moon and Mars are commonly large, have flat floors and typically lack central peaks [*Schultz*, 1976; *Schultz and Orphal*, 1978]. Several previous studies [e.g., *Cintala and Grieve*, 1998; *Melosh*, 1989; *Pierazzo et al.*, 1997] predict the formation of impact melt in the bottom of craters and predict that the mass of the impact melt that remains in the crater makes up a larger proportion of the total mass displaced as crater size increases,

independent of material strength or gravity. Many of the identified high thermal inertia surfaces are located within large craters, and it is expected that these craters have large amounts of impact melt (typically >500 $km^3$ for impacts with a transient cavity >50 km in diameter) [e.g., *Cintala and Grieve*, 1998; *Melosh*, 1989; *Pierazzo et al.*, 1997].

[51] Although large volumes of impact melt are likely generated in these cases, the cause of the flat crater floors may be due to inflationary volcanism that follows fractures in the basement rock derived from the impact event [*Schultz*, 1976; *Schultz and Orphal*, 1978]. In this scenario, a sill or dike from a nearby preexisting magma chamber or a new magma body created by the unloading and partial melting of the underlying mantle intersects the fractured zone beneath the impact crater. A new sill begins to form at the base of the highly fractured basement rock, which begins to inflate the floor of the crater, fed by the tapped magma body [*Schultz*, 1976]. This inflation has the effect of decreasing the overall topographic relief of the crater floor and may also reduce topographic relief of the central peak, leading to the flat floors observed [*Schultz*, 1976]. Subsequently, dikes can make their way to the surface and depending on the degree basement fracture, may erupt (typically mafic) lavas onto the surface of the uplifted crater, potentially obscuring the original crater floor, including the central peak [*Schultz*, 1976]. The fractures and graben commonly observed in these craters may be surface manifestations of subsurface fractures in the basement rock caused by the impact event or they may be related to subsequent modification [*Newsom*, 1980].

[52] While the composition of Martian and lunar crater deposits have not been constrained globally, the composition of several craters in the Mare Serpentis region of Mars have been examined and were found to be significantly more mafic than the surrounding intercrater units [*Rogers et al.*, 2009]. The impact process may remelt the regolith in the area and form consolidated rock with a similar composition to the bulk local crust. If the impact event resulted in a volcanic eruption, the composition of this lava may be representative of the bulk crust or the mantle if partial melting is the source of the magma. It may also be possible, depending on cooling rates, for large volumes of impact melt glass to form. Depending on the rates of devitrification, this glassy material may still be observable in spectroscopic investigations. Reflectance spectroscopic studies of several large lunar highlands craters have identified rapidly recrystallized impact melt and Fe-bearing impact melt glass [*Smrekar and Pieters*, 1985].

[53] The morphologies associated with Martian high thermal inertia craters, such as rough and pitted textures, in addition to the lack of layered material observed, indicate that the floors of these craters are not simply infilled by sediments, as is the case with the layered deposits in Gale Crater [e.g., *Malin and Edgett*, 2000; *Pelkey et al.*, 2004]. Since high thermal inertia craters are likely not covered by dust or other sediments, the wind must be strong enough to prevent mantling.

[54] It is possible to make general comparisons between the high thermal inertia intracrater material of *Christensen* [1983] and the bedrock distribution. Although the resolution of the map produced by *Christensen* [1983] is insufficient to make a direct global comparison, most craters appear to be located in regions similar to those where bedrock has been identified. *Christensen* [1983] mapped a region near Iapygia at higher resolution, allowing a direct comparison to the bedrock distribution. This area has dark, high thermal inertia splotches identified by *Christensen* [1983] and 10 of ~110 high thermal inertia splotches correspond directly to bedrock locations identified here with THEMIS. There are no instances where bedrock is not associated with these low-albedo, high thermal inertia splotches, but there are significantly more intracrater deposits identified than crater floor bedrock instances in this area. It is possible that these splotches, which commonly occur on the downwind side of the crater [*Arvidson*, 1974; *Christensen*, 1983], may be aeolian deposits derived from the high thermal inertia crater floor material. If this is the case, then high thermal inertia material is closely associated with scouring by wind, which then transports the eroded material to the downwind side of the crater, where the sediment can exhibit bed forms observed in this study and by others [*Arvidson*, 1974; *Christensen*, 1983]. However, it is also possible that the splotches are the bedrock surface and are not aeolian deposits. It is difficult to constrain which case is the most likely, as the resolution of the data used by *Christensen* [1983] is too low for the distinction to be made.

[55] Most occurrences of the crater floor surface type have little or no associated aeolian material in the crater, except for localized occurrences in topographic lows and fractures. However, the high thermal inertia surface can have an eroded and rough texture, which implies an active or recently active aeolian process to help keep the surface free of mantling materials.

### 4.4. Intercrater Surfaces

[56] A variety of studies have characterized several of the high thermal inertia intercrater surfaces compositionally, thermophysically, and morphologically [e.g., *Christensen et al.*, 2003; *Edwards et al.*, 2008; *Hamilton and Christensen*, 2005; *Mustard et al.*, 2007; *Rogers et al.*, 2009]. This surface type occurs in a variety of locations with no clearly distinguishable formation mechanism common to these instances. The surface textures and exhumed morphology of this surface type indicate that an active or recently active aeolian process is scouring the surface and removing mantling material. When these surfaces are viewed at small scales (Figure 7d), individual cobbles and boulders can be seen that are likely derived from the in-place bedrock. This type of morphology is similar among many of these surfaces, indicating that they may preferentially weather into blocky material before becoming finer grained.

[57] In addition to the blocky material, fractures are also observed in these surfaces, but are not as prevalent and are typically larger than those observed in the crater floor high thermal inertia surface type. The larger scale of the fractures, as well as their preferential orientation, may be indicative of regional tectonic stresses. The fractures visible in Figures 7a–7c show a lower thermal inertia material filling the fractures. This material exhibits bed forms and is likely sedimentary material that preferentially collects in topographic lows.

[58] The primary geologic origin of high thermal inertia intercrater surfaces is also not well understood and may not be the same for each instance. These surfaces seem to have a variety of small-scale morphologies associated with them, but most have similar properties, such as their blocky nature. The pitted and rough textures may indicate aeolian processes,

which scour mantling material from the surface, revealing the underlying bedrock, or it may be related to the texture of the original deposit. In addition to these similar morphologies, many studies [e.g., *Bandfield and Rogers*, 2008; *Christensen et al.*, 2003; *Edwards et al.*, 2008; *Hamilton and Christensen*, 2005; *Hoefen et al.*, 2003; *Mustard et al.*, 2007; *Rogers et al.*, 2005, 2009] have characterized the compositional nature of a variety of these surfaces, finding them to be typically dominated by basaltic materials, with significant concentrations of plagioclase, pyroxene, and olivine.

[59] In-place material and outcrops observed at the MER landing sites do not typically qualify as bedrock in this study. Mini-TES derived thermal inertia values indicate that only the basaltic rocks (e.g., Bonneville Beacon) at Gusev crater are consistent with the definition of bedrock in this study, while the Columbia Hills have significantly lower values (e.g., $\sim$620 J m$^{-2}$ K$^{-1}$ s$^{-1/2}$) [*Fergason et al.*, 2006b]. This implies that the induration or lithification of sediments (such as those that compose the Columbia Hills) is not an applicable formation mechanism for surfaces examined in this study [e.g., *Arvidson et al.*, 2006; *McCoy et al.*, 2008; *McSween et al.*, 2006]. This may also indicate that these surfaces are likely composed of crystalline volcanic rocks, which have not been significantly altered, reworked, or mantled.

[60] *Rogers et al.* [2009] have characterized a representative portion of the southern cratered highlands in Mare Serpentis, to better understand the geologic history of the highlands. *Rogers et al.* [2009] have used TES, THEMIS, and Mars Express Observatoire pour la Minéralogie, l'Eau, les Glaces, et l'Activité (OMEGA) [*Bibring et al.*, 2005] data to characterize the compositional nature of the high thermal inertia intercrater units in this area, identifying them as being relatively olivine- and pyroxene-rich. These outcrops are typically isolated exposures of mafic bedrock, which are surrounded by less mafic, lower thermal inertia plains [*Rogers et al.*, 2009]. *Rogers et al.* [2009] propose two possible relationships between the intercrater high thermal inertia unit and the lower inertia unit: either (1) the mechanical and/or chemical weathering of mafic bedrock to form the surrounding lower thermal inertia highlands material or (2) the initial formation of two distinct lithologies [*Rogers et al.*, 2009]. The former relationship correlates well with what is observed in Argyre Planitia, Gusev Crater, Nili Fossae and the southern rim of Isidis Basin, where olivine-rich material is altered to olivine-poor material in the process of mechanical weathering [*Bandfield and Rogers*, 2008]. *Bandfield and Rogers* [2008] propose that this process may be widespread on Mars and that the primary igneous compositions are typically more mafic, subsequently becoming olivine-poor through dissolution by acidic fluids. The few locations of in-place intercrater bedrock seem to be largely mafic in nature relative to the surrounding lower-inertia regolith.

## 5. Conclusions

[61] In this study, we have shown the following.

[62] 1. Mars has remarkably few exposures of bedrock on a 100 m scale. The majority of high thermal inertia surfaces occur in the cratered southern highlands and/or low-albedo regions and not in high-albedo dust-mantled regions. This observation leads to the possibility that Mars has experienced large-scale crustal processing and reworking, which has destroyed or masked bedrock.

[63] 2. Bedrock exposures are nearly nonexistent at high latitudes (poleward of 45°N and 58°S). This lack of bedrock is likely due to enhanced mechanical breakdown of material associated with the distribution of permafrost at higher latitudes [e.g., *Bandfield and Feldman*, 2008; *Kreslavsky et al.*, 2008]. Periglacial processes may have progressively broken down materials to form the Martian regolith in these areas.

[64] 3. Three distinct surface morphologies of high thermal inertia have been identified and classified as valley and crater wall, crater floor, and intercrater surfaces. These morphologies are indicative of different formation and exposure mechanisms.

[65] 4. The valley and crater wall surface morphology implies a significant amount of erosion and mass wasting with limited subsequent deposition due to the high surface slope angles (often >27°). This type of morphology is the most commonly observed high thermal inertia surface.

[66] 5. Crater floor high surfaces have morphologies (e.g., flat and fractured floors, generally large diameters, and few central peaks) similar to Lunar craters where impact melt has been identified [e.g., *Smrekar and Pieters*, 1985; *Wilhelms et al.*, 1987]. Impact melt can also be expected based on numerical models and can be related to the size of the transient cavity and impact velocity [e.g., *Cintala and Grieve*, 1998; *Melosh*, 1989; *Pierazzo et al.*, 1997]. This surface type is most likely associated with inflationary volcanism as a result of large impact events, where magma reaches the surface through fractures in the basement rock caused by the impact [*Schultz*, 1976; *Schultz and Glicken*, 1979]. Rough and pitted textures may imply recent aeolian processes, which scour mantling materials and expose the underlying high thermal inertia surfaces.

[67] 6. The intercrater surface type, which is not associated with significant topographic relief, has rough textures along with an exhumed morphology that imply an active or recently active erosional aeolian process.

[68] 7. This as well as other studies [*Bandfield and Rogers*, 2008; *Rogers et al.*, 2009], indicate a distinct correlation between high thermal inertia surfaces and compositions significantly more mafic than the surrounding regolith. This correlation may indicate that chemical weathering processes are commonly associated with the formation of the Martian regolith.

[69] **Acknowledgments.** The authors would like to thank H. H. Kieffer for providing the KRC thermal model, Deanne Rogers for helpful comments and discussion, and the JMARS software development team for providing software that aided in the analysis of and access to data presented in this work. Additionally, the authors would like to thank the THEMIS mission planners and support staff for providing targeting opportunities and helpful discussion and Nathaniel Putzig and an anonymous referee for reviews, which improved the manuscript. This work was funded by the NASA 2001 Mars Odyssey THEMIS project.

## References

Armstrong, J. C., T. N. Titus, and H. H. Kieffer (2005), Evidence for subsurface water ice in Korolev crater, Mars, *Icarus*, *174*(2), 360–372, doi:10.1016/j.icarus.2004.10.032.

Arvidson, R. E. (1974), Wind-blown streaks, splotches, and associated craters on Mars: Statistical analysis of Mariner 9 photographs, *Icarus*, *21*(1), 12–27, doi:10.1016/0019-1035(74)90086-4.

Arvidson, R. E., et al. (2006), Overview of the Spirit Mars Exploration Rover mission to Gusev Crater: Landing site to Backstay Rock in the Columbia Hills, *J. Geophys. Res.*, *111*, E02S01, doi:10.1029/2005JE002499.

Bandfield, J. L. (2007), High-resolution subsurface water-ice distributions on Mars, *Nature*, *447*, 64–67, doi:10.1038/nature05781.

Bandfield, J. L., and W. C. Feldman (2008), Martian high latitude permafrost depth and surface cover thermal inertia distributions, *J. Geophys. Res.*, *113*, E08001, doi:10.1029/2007JE003007.

Bandfield, J. L., and A. D. Rogers (2008), Olivine dissolution by acidic fluids in Argyre Planitia, Mars: Evidence for a widespread process?, *Geology*, *36*(7), 579–582, doi:10.1130/G24724A.1.

Bandfield, J. L., D. Rogers, M. D. Smith, and P. R. Christensen (2004), Atmospheric correction and surface spectral unit mapping using Thermal Emission Imaging System data, *J. Geophys. Res.*, *109*, E10008, doi:10.1029/2004JE002289.

Basu, S., M. I. Richardson, and R. J. Wilson (2004), Simulation of the Martian dust cycle with the GFDL Mars GCM, *J. Geophys. Res.*, *109*, E11006, doi:10.1029/2004JE002243.

Bibring, J.-P., et al. (2005), Mars surface diversity as revealed by the OMEGA/Mars Express observations, *Science*, *307*(5715), 1576–1581, doi:10.1126/science.1108806.

Bruno, B. C., S. A. Fagents, C. W. Hamilton, D. M. Burr, and S. M. Baloga (2006), Identification of volcanic rootless cones, ice mounds, and impact craters on Earth and Mars: Using spatial distribution as a remote sensing tool, *J. Geophys. Res.*, *111*, E06017, doi:10.1029/2005JE002510.

Christensen, P. R. (1982), Martian dust mantling and surface composition: Interpretation of thermophysical properties, *J. Geophys. Res.*, *87*(B12), 9985–9998, doi:10.1029/JB087iB12p09985.

Christensen, P. R. (1983), Eolian intracrater deposits on Mars: Physical properties and global distribution, *Icarus*, *56*(3), 496–518, doi:10.1016/0019-1035(83)90169-0.

Christensen, P. R. (1988), Global albedo variations on Mars: Implications for active aeolian transport, deposition, and erosion, *J. Geophys. Res.*, *93*(B7), 7611–7624, doi:10.1029/JB093iB07p07611.

Christensen, P. R., and H. J. Moore (1992), The Martian surface layer, in *Mars*, edited by H. H. Kieffer et al., pp. 686–729, Univ. of Ariz. Press, Tucson.

Christensen, P. R., et al. (2003), Morphology and composition of the surface of Mars: Mars Odyssey THEMIS results, *Science*, *300*(5628), 2056–2061, doi:10.1126/science.1080885.

Christensen, P. R., et al. (2004), The Thermal Emission Imaging System (THEMIS) for the Mars 2001 Odyssey mission, *Space Sci. Rev.*, *110*(1–2), 85–130, doi:10.1023/B:SPAC.0000021008.16305.94.

Christensen, P. R., et al. (2005a), Evidence for magmatic evolution and diversity on Mars from infrared spectral observations, *Nature*, *436*, 504–509, doi:10.1038/nature03639.

Christensen, P. R., et al. (2005b), Mars Exploration Rover candidate landing sites as viewed by THEMIS, *Icarus*, *176*(1), 12–43, doi:10.1016/j.icarus.2005.01.004.

Christensen, P., N. Gorelick, S. Anwar, S. Dickenshied, C. Edwards, E. Engle, and T. S. Team (2007), New insights about Mars from the creation and analysis of Mars global datasets, *Eos Trans. AGU*, *88*(52), Fall Meet. Suppl., Abstract P11E-01.

Cintala, M. J., and R. A. F. Grieve (1998), Scaling impact-melt and crater dimensions: Implications for the lunar cratering record, *Meteorit. Planet. Sci.*, *33*(4), 889–912.

Clancy, R. T., S. W. Lee, G. R. Gladstone, W. W. McMillan, and T. Rousch (1995), A new model for Mars atmospheric dust based upon analysis of ultraviolet through infrared observations from Mariner 9, Viking, and Phobos, *J. Geophys. Res.*, *100*(E3), 5251–5263, doi:10.1029/94JE01885.

Edwards, C. S., P. R. Christensen, and V. E. Hamilton (2008), Evidence for extensive olivine-rich basalt bedrock outcrops in Ganges and Eos chasmas, Mars, *J. Geophys. Res.*, *113*, E11003, doi:10.1029/2008JE003091.

Feldman, W. C., et al. (2002), Global distribution of neutrons from Mars: Results from Mars Odyssey, *Science*, *297*(5578), 75–78, doi:10.1126/science.1073541.

Fenton, L. K., and M. I. Richardson (2001), Martian surface winds: Insensitivity to orbital changes and implications for aeolian processes, *J. Geophys. Res.*, *106*(E12), 32,885–32,901, doi:10.1029/2000JE001407.

Fergason, R. L., P. R. Christensen, and H. H. Kieffer (2006a), High-resolution thermal inertia derived from the Thermal Emission Imaging System (THEMIS): Thermal model and applications, *J. Geophys. Res.*, *111*, E12004, doi:10.1029/2006JE002735.

Fergason, R. L., P. R. Christensen, J. F. Bell III, M. P. Golombek, K. E. Herkenhoff, and H. H. Kieffer (2006b), Physical properties of the Mars Exploration Rover landing sites as inferred from Mini-TES–derived thermal inertia, *J. Geophys. Res.*, *111*, E02S21, doi:10.1029/2005JE002583.

Gerstell, M. F., O. Aharonson, and N. Schorghofer (2004), A distinct class of avalanche scars on Mars, *Icarus*, *168*(1), 122–130, doi:10.1016/j.icarus.2003.11.005.

Golombek, M. P., et al. (2006), Erosion rates at the Mars Exploration Rover landing sites and long-term climate change on Mars, *J. Geophys. Res.*, *111*, E12S10, doi:10.1029/2006JE002754.

Greeley, R., N. T. Bridges, D. A. Crown, L. S. Crumpler, S. A. Fagents, P. J. Mouginis-Mark, and J. R. Zimbelman (2000), Volcanism on the red planet: Mars, in *Environmental Effects on Volcanic Eruptions: From Deep Oceans to Deep Space*, edited by J. R. Zimbelman and T. K. P. Gregg, chap. 4, pp. 75–112, Plenum, New York.

Hamilton, V. E., and P. R. Christensen (2005), Evidence for extensive, olivine-rich bedrock on Mars, *Geology*, *33*(6), 433–436, doi:10.1130/G21258.1.

Hoefen, T. M., R. N. Clark, J. L. Bandfield, M. D. Smith, J. C. Pearl, and P. R. Christensen (2003), Discovery of olivine in the Nili Fossae region of Mars, *Science*, *302*(5645), 627–630, doi:10.1126/science.1089647.

Jakosky, B. M. (1986), On the thermal properties of Martian fines, *Icarus*, *66*(1), 117–124, doi:10.1016/0019-1035(86)90011-4.

Jakosky, B. M., B. G. Henderson, and M. T. Mellon (1995), Chaotic obliquity and the nature of the Martian climate, *J. Geophys. Res.*, *100*(E1), 1579–1584, doi:10.1029/94JE02801.

Kieffer, H. H., S. C. Chase Jr., E. Miner, G. Münch, and G. Neugebauer (1973), Preliminary report on infrared radiometric measurements from the Mariner 9 spacecraft, *J. Geophys. Res.*, *78*(20), 4291–4312, doi:10.1029/JB078i020p04291.

Kieffer, H. H., T. Z. Martin, A. R. Peterfreund, B. M. Jakosky, E. D. Miner, and F. D. Palluconi (1977), Thermal and albedo mapping of Mars during the Viking primary mission, *J. Geophys. Res.*, *82*(28), 4249–4291, doi:10.1029/JS082i028p04249.

Kreslavsky, M. A., J. W. Head, and D. R. Marchant (2008), Periods of active permafrost layer formation during the geological history of Mars: Implications for circum-polar and mid-latitude surface processes, *Planet. Space Sci.*, *56*(2), 289–302, doi:10.1016/j.pss.2006.02.010.

Lanagan, P. D., A. S. McEwen, L. P. Keszthelyi, and T. Thordarson (2001), Rootless cones on Mars indicating the presence of shallow equatorial ground ice in recent times, *Geophys. Res. Lett.*, *28*(12), 2365–2367, doi:10.1029/2001GL012932.

Malin, M. C., and K. S. Edgett (2000), Sedimentary rocks of early Mars, *Science*, *290*(5498), 1927–1937, doi:10.1126/science.290.5498.1927.

Malin, M. C., et al. (1998), Early views of the Martian surface from the Mars Orbiter Camera of Mars Global Surveyor, *Science*, *279*(5357), 1681–1685, doi:10.1126/science.279.5357.1681.

McCoy, T. J., et al. (2008), Structure, stratigraphy, and origin of Husband Hill, Columbia Hills, Gusev Crater, Mars, *J. Geophys. Res.*, *113*, E06S03, doi:10.1029/2007JE003041.

McEwen, A. S., et al. (2007), Mars Reconnaissance Orbiter's High Resolution Imaging Science Experiment (HiRISE), *J. Geophys. Res.*, *112*, E05S02, doi:10.1029/2005JE002605.

McSween, H. Y., et al. (2006), Alkaline volcanic rocks from the Columbia Hills, Gusev Crater, Mars, *J. Geophys. Res.*, *111*, E09S91, doi:10.1029/2006JE002698.

Mellon, M. T., and B. M. Jakosky (1995), The distribution and behavior of Martian ground ice during past and present epochs, *J. Geophys. Res.*, *100*(E6), 11,781–11,799, doi:10.1029/95JE01027.

Mellon, M. T., B. M. Jakosky, H. H. Kieffer, and P. R. Christensen (2000), High-resolution thermal inertia mapping from the Mars Global Surveyor Thermal Emission Spectrometer, *Icarus*, *148*(2), 437–455, doi:10.1006/icar.2000.6503.

Mellon, M. T., R. L. Fergason, and N. E. Putzig (2008), The thermal inertia of the surface of Mars, in *The Martian Surface: Composition, Mineralogy, and Physical Properties*, edited by J. Bell, pp. 399–427, Cambridge Univ. Press, New York.

Melosh, H. J. (1989), *Impact Cratering: A Geologic Process*, 245 pp., Oxford Univ. Press, New York.

Mitrofanov, I., et al. (2002), Maps of subsurface hydrogen from the high energy neutron detector, Mars Odyssey, *Science*, *297*(5578), 78–81, doi:10.1126/science.1073616.

Mustard, J. F., F. Poulet, J. W. Head, N. Mangold, J.-P. Bibring, S. M. Pelkey, C. I. Fassett, Y. Langevin, and G. Neukum (2007), Mineralogy of the Nili Fossae region with OMEGA/Mars Express data: 1. Ancient impact melt in the Isidis Basin and implications for the transition from the Noachian to Hesperian, *J. Geophys. Res.*, *112*, E08S03, doi:10.1029/2006JE002834.

Newsom, H. E. (1980), Hydrothermal alteration of impact melt sheets with implications for Mars, *Icarus*, *44*(1), 207–216, doi:10.1016/0019-1035(80)90066-4.

Paige, D. A., J. E. Bachman, and K. D. Keegan (1994), Thermal and albedo mapping of the polar regions of Mars using Viking thermal mapper observations: 1. North polar region, *J. Geophys. Res.*, *99*(E12), 25,959–25,991, doi:10.1029/93JE03428.

Palluconi, F. D., and H. H. Kieffer (1981), Thermal inertia mapping of Mars from 60°S to 60°N, *Icarus*, *45*(2), 415–426, doi:10.1016/0019-1035(81)90044-0.

Pelkey, S. M., B. M. Jakosky, and P. R. Christensen (2004), Surficial properties in Gale Crater, Mars, from Mars Odyssey THEMIS data, *Icarus*, *167*(2), 244–270, doi:10.1016/j.icarus.2003.09.013.

Pierazzo, E., A. M. Vickery, and H. J. Melosh (1997), A reevaluation of impact melt production, *Icarus*, *127*(2), 408–423, doi:10.1006/icar.1997.5713.

Pollack, J. B., D. S. Colburn, F. M. Flasar, R. Kahn, C. E. Carlston, and D. Pidek (1979), Properties and effects of dust particles suspended in the Martian atmosphere, *J. Geophys. Res.*, *84*(B6), 2929–2945, doi:10.1029/JB084iB06p02929.

Presley, M. A., and P. R. Christensen (1997a), The effect of bulk density and particle size sorting on the thermal conductivity of particulate materials under Martian atmospheric pressures, *J. Geophys. Res.*, *102*(E4), 9221–9229, doi:10.1029/97JE00271.

Presley, M. A., and P. R. Christensen (1997b), Thermal conductivity measurements of particulate materials: 2. Results, *J. Geophys. Res.*, *102*(E3), 6551–6566, doi:10.1029/96JE03303.

Presley, M. A., and P. R. Christensen (1997c), Thermal conductivity measurements of particulate materials: 1. A review, *J. Geophys. Res.*, *102*(E3), 6535–6549, doi:10.1029/96JE03302.

Presley, M. A., and R. A. Craddock (2006), Thermal conductivity measurements of particulate materials: 3. Natural samples and mixtures of particle sizes, *J. Geophys. Res.*, *111*, E09013, doi:10.1029/2006JE002706.

Putzig, N. E., and M. T. Mellon (2007a), Thermal behavior of horizontally mixed surfaces on Mars, *Icarus*, *191*(1), 52–67, doi:10.1016/j.icarus.2007.03.022.

Putzig, N. E., and M. T. Mellon (2007b), Apparent thermal inertia and the surface heterogeneity of Mars, *Icarus*, *191*(1), 68–94, doi:10.1016/j.icarus.2007.05.013.

Putzig, N. E., M. T. Mellon, K. A. Kretke, and R. E. Arvidson (2005), Global thermal inertia and surface properties of Mars from the MGS mapping mission, *Icarus*, *173*(2), 325–341, doi:10.1016/j.icarus.2004.08.017.

Rogers, A. D., P. R. Christensen, and J. L. Bandfield (2005), Compositional heterogeneity of the ancient Martian crust: Analysis of Ares Vallis bedrock with THEMIS and TES data, *J. Geophys. Res.*, *110*, E05010, doi:10.1029/2005JE002399.

Rogers, A. D., O. Aharonson, and J. L. Bandfield (2009), Geologic context of in situ rocky exposures in Mare Serpentis, Mars: Implications for crust and regolith evolution in the cratered highlands, *Icarus*, *200*(2), 446–462, doi:10.1016/j.icarus.2008.11.026.

Ruff, S. W., and P. R. Christensen (2002), Bright and dark regions on Mars: Particle size and mineralogical characteristics based on Thermal Emission Spectrometer data, *J. Geophys. Res.*, *107*(E12), 5127, doi:10.1029/2001JE001580.

Schultz, P. H. (1976), Floor-fractured lunar craters, *Earth Moon Planets*, *15*(3), 241–273.

Schultz, P. H., and H. Glicken (1979), Impact crater and basin control of igneous processes on Mars, *J. Geophys. Res.*, *84*(B14), 8033–8047, doi:10.1029/JB084iB14p08033.

Schultz, P. H., and D. L. Orphal (1978), Floor-fractured craters on the moon and Mars, *Meteoritics*, *13*, 622–625.

Smith, M. D., J. C. Pearl, B. J. Conrath, and P. R. Christensen (2001), Thermal Emission Spectrometer results: Mars atmospheric thermal structure and aerosol distribution, *J. Geophys. Res.*, *106*(E10), 23,929–23,945, doi:10.1029/2000JE001321.

Smith, M. D., J. L. Bandfield, P. R. Christensen, and M. I. Richardson (2003), Thermal Emission Imaging System (THEMIS) infrared observations of atmospheric dust and water ice cloud optical depth, *J. Geophys. Res.*, *108*(E11), 5115, doi:10.1029/2003JE002115.

Smrekar, S., and C. M. Pieters (1985), Near-infrared spectroscopy of probable impact melt from three large lunar highland craters, *Icarus*, *63*(3), 442–452, doi:10.1016/0019-1035(85)90056-9.

Sullivan, R. J. (1992), Evolution of steep Martian slopes, Ph.D. thesis, Ariz. State Univ., Tempe.

Sullivan, R., P. Thomas, J. Veverka, M. Malin, and K. S. Edgett (2001), Mass movement slope streaks imaged by the Mars Orbiter Camera, *J. Geophys. Res.*, *106*(E10), 23,607–23,633, doi:10.1029/2000JE001296.

Titus, T. N., H. H. Kieffer, and P. R. Christensen (2003), Exposed water ice discovered near the south pole of Mars, *Science*, *299*(5609), 1048–1051, doi:10.1126/science.1080497.

Wilhelms, D. E., J. F. McCauley, and N. J. Trask (1987), *The Geologic History of the Moon*, *U.S. Geol. Surv. Prof. Pap., 1348*, 302 pp.

J. L. Bandfield, Department of Earth and Space Sciences, University of Washington, Johnson Hall 070, Box 351310, 4000 15th Avenue NE, Seattle, WA 98195-1310, USA.

P. R. Christensen and C. S. Edwards, Mars Space Flight Facility, School of Earth and Space Exploration, Arizona State University, P.O. Box 876305, Tempe, AZ 85287-6305, USA. (christopher.edwards@asu.edu)

R. L. Fergason, Astrogeology Team, U.S. Geological Survey, 2255 North Gemini Drive, Flagstaff, AZ 86001, USA.